Measurement report: Hygroscopicity of Size-Selected Aerosol Particles in the Heavily Polluted Urban Atmosphere of Delhi: Impacts of Chloride Aerosol

Anil Kumar Mandariya[1,2], Ajit Ahlawat[3], Mohd. M. V. Haneef[1], Nisar A. Baig[1], Kanan Patel[4], Joshua S. Apte[5], Lea Hildebrandt Ruiz[4], Alfred Wiedensohler[3]*, and Gazala Habib[1]*

[1]Department of Civil Engineering, Indian Institute of Technology Delhi, New Delhi, India

[2]now at: Univ Paris Est Creteil and University Paris Cité, CNRS, LISA, F – 94010 Créteil, France

[3]Leibniz Institute for Tropospheric Research (TROPOS), Permoserstraße, 15 Leipzig, Germany

[4]Department of Civil, Architectural and Environmental Engineering, The University of Texas at Austin, Austin, Texas, USA

[5]McKetta Department of Chemical Engineering, The University of Texas at Austin, Austin, Texas, USA

Correspondence to: Gazala Habib (gazalahabib@civil.iitd.ac.in) and Alfred Wiedensohler (ali@tropos.de)

Abstract. Recent research has revealed the crucial role of winter-time, episodic high chloride (H-Cl) emissions in the Delhi region, which significantly impact aerosol hygroscopicity and aerosol-bound liquid water, thus contributing to the initiation of Delhi fog episodes. However, these findings have primarily relied on modeled aerosol hygroscopicity, necessitating validation through direct hygroscopicity measurements. This study presents the measurements of non-refractory bulk aerosol composition of PM_1 from an Aerodyne aerosol chemical speciation monitor and for first-time size-resolved hygroscopic growth factors (Nucleation, Aitken, and Accumulated mode particles) along with their associated hygroscopicity parameters at 90% relative humidity using a hygroscopic-tandem differential mobility analyzer at the Delhi Aerosol Supersite. Our observations demonstrate that the hygroscopicity parameter for aerosol particles varies from 0.00 to 0.11 (with an average of 0.03 ± 0.02) for 20 nm particles, 0.05 to 0.22 (0.11 ± 0.03) for 50 nm particles, 0.05 to 0.30 (0.14 ± 0.04) for 100 nm particles, 0.05 to 0.41 (0.18 ± 0.06) for 150 nm particles, and 0.05 to 0.56 (0.22 ± 0.07) for 200 nm particles. Surprisingly, our findings demonstrate that the period with H-Cl emissions displays notably greater hygroscopicity (0.35 ± 0.06) in comparison to spans marked by high biomass burning (0.18 ± 0.04), high hydrocarbon-like organic aerosol (0.17 ± 0.05), and relatively cleaner periods (0.27 ± 0.07). This research presents initial observational proof that ammonium chloride is the main factor behind aerosol hygroscopic growth and aerosol-bound liquid water content in Delhi. The finding emphasizes, ammonium chloride's role in aerosol-water interaction and related haze/fog development. Moreover, the high chloride levels in aerosols seem to prevent the adverse impact of high organic aerosol concentrations on cloud condensation nuclei activity.

1. Introduction

The Intergovernmental Panel on Climate Change (IPCC) (Intergovernmental Panel on Climate Change, 2023) reported that the interaction between aerosols and clouds is not completely comprehended, and there are significant uncertainties in gauging global radiative budgets. In order to overcome and elucidate these uncertainties, the role of aerosol hygroscopicity is crucial. Hygroscopicity is a critical factor in comprehendling how aerosol particles functions as cloud condensation nuclei (CCN) and create fog droplets/haze under sub-saturated/nearly saturation conditions, as well as forming cloud droplets at atmospheric supersaturation levels (McFiggans et al., 2006; Topping and McFiggans, 2012). Its comprehension is vital to better predicting the aerosol size distribution and scattering properties with more accuracy in global models under varying atmospheric humidity (RH) conditions (Randall et al., 2007). Hygroscopicity at higher RH results in an increase in the cross-sectional area of the aerosol, leading to efficient light scattering by the aerosol particles (Tang and Munkelwitz, 1994). This phenomenon is primarily dependent on the chemical composition and particle size. Generally, ammonium salts of sulfate, nitrate, and chloride, which are inorganic salts, exhibit high hygroscopicity (Hu et al., 2011; Petters and Kreidenweis, 2007). In contrast, organic aerosols (OAs) have relatively lower hygroscopicity (Jimenez et al., 2009; Kroll et al., 2011), and dust particles and black/elemental carbon particles are known to be hydrophobic (Seinfeld and Pandis, 2006). The increased atmospheric humidity during winter and monsoon seasons promotes the development of more oxidized secondary organic aerosol (SOA) through aqueous-phase (Ervens et al., 2011) and heterogeneous reactions (McNeill, 2015). This process leads to a heightened organic aerosol hygroscopicity (Jimenez et al., 2009; Mei et al., 2013), which negatively impacts the local visibility (Li et al., 2016; Liu et al., 2012). Conversely, aerosol loading has an inverse effect on aerosol hygroscopicity (Mandariya et al., 2020a). In addition, aerosol loading plays a critical role in determining cloud lifetime, which impacts the amount of rainfall in the region (Albrecht, 1989; Lohmann and Feichter, 2005).

Over the past few decades, researchers have extensively measured aerosol hygroscopicity using a hygroscopic tandem differential mobility analyzer (H-TDMA) (Massling et al., 2005; Gysel et al., 2007; Mandariya et al., 2020; Swietlicki et al., 2008; Yeung et al., 2014; Kecorius et al., 2019) and a CCN counter (Bhattu and Tripathi, 2015; Gunthe et al., 2011; Massoli et al., 2010; Ogawa et al., 2016) under sub- and supersaturated conditions, respectively. Petters and Kreidenweis (2007) introduced the hygroscopicity parameter, kappa (κ), to correlate aerosol hygroscopicity with its chemical composition. Hygroscopicity of OA may differ according to their chemical properties such as solubility, extent of dissociation in aerosol water, and surface activity, which can pose

62 challenges in quantifying OA hygroscopicity (Hallquist et al., 2009; Jimenez et al., 2009). As a result, this

63 introduces further discrepancies in predicted and measured aerosol hygroscopicity. Therefore, there is a

64 requirement to investigate the measurement-based aerosol hygroscopicity of Delhi's atmosphere to gain a better

65 understanding of the recurring occurrences of haze and cloud formations.

66 In recent decades, rapid economic growth and industrialization in the Indo-Gangetic Plain (IGP) have resulted in

67 significantly poor air quality during the winter season (Wester et al., 2019). Local and regional air pollution issues

68 may potentially affect Delhi during this time (Arub et al., 2020; Bhandari et al., 2020; Gani et al., 2019; Prakash

69 et al., 2018). Recent studies have indicated that chloride significantly contributes to the degradation of air quality

70 in the Delhi region and favors haze/fog formation during winter (Gunthe et al., 2021). Gani et al. (2019) and Rai

71 et al. (2020) support these findings. Trash and biomass burning for heating and waste degradation have been

72 identified as major sources of chloride in Delhi (Rai et al., 2020). A recent study conducted in Delhi revealed that

73 frequent high chloride events promote high levels of aerosol liquid water content under elevated humid conditions.

74 This leads to haze and poor visibility in the city (Chen et al., 2022). Additionally, Gunthe et al. (2021) found that

75 higher chloride levels also enhance aerosol hygroscopicity. However, it is important to note that this particular

76 study was based on theoretical hygroscopicity. Therefore, it is crucial to study the effects of chloride on aerosol

77 hygroscopicity and its ability to increase the amount of aerosol-bound liquid water based on field measurements.

78 In addition, the heavily polluted urban atmosphere, with its highly complex composition, severely limits the

79 hygroscopicity of the aerosol particles. This is particularly evident in cities like Delhi, located in the IGP of India,

80 where air quality deteriorates significantly during haze/fog-dominated periods. To the author's best knowledge,

81 this study is the first to explore the complex atmosphere of IGP in Delhi, India, using aerosol hygroscopicity

82 measured by H-TDMA.

83 **2. Experimental Methods**

84 **2.1 Aerosol Measurements**

85 Real-time measurements of atmospheric aerosols were conducted during winter (February 1, 2020 to March 20,

86 2020) at Indian Institute of Technology (IIT) Delhi, Block 5. H-TDMA, TROPOS-type Mobility Particle Size

87 Spectrometer (MPSS), and Aerodyne Aerosol Chemical Speciation Monitor (ACSM) from Aerodyne Research

88 in Billerica, MA were used simultaneously at a height of approximately 15 meters above ground level (a.g.l.) as

89 depicted in Fig. 1. Lab-2 is located 50 meters away from Lab-1. The ACSM is utilized to quantify mass

90 concentrations of organic aerosol (OA), ammonium (NH$_4$), sulfate (SO$_4$), nitrate (NO$_3$), and chloride (Cl) in non-

91 refractory particulate matter less than 1 μm (NR-PM$_1$).

92 The hygroscopic growth of size-resolved particles at 90 % RH was investigated using the HTDMA system in this

93 study. The HTDMA system has been utilized in numerous field campaigns before (Massling et al., 2007; Wu et

94 al., 2013b; Zhang et al., 2016). The HTDMA system (TROPOS, Germany) consists of two Differential Mobility

95 Analyzers (DMAs) of the Hauke-median type (TROPOS, Germany), along with a Condensation Particle Counter

96 (CPC) Model 3772 by TSI Inc. (USA), and a humidifier system situated between the two DMAs. The initial

97 DMA's function is to choose quasi-monodisperse particles at a dry diameter (D$_p$, dry) of 30% RH. Technical

98 abbreviations will be explicated at their first usage. After passing through a humidity conditioner, the humidity of

99 the size-selected particles can be adjusted from 30% to 90% RH by mixing dry air with RH<5% and moist air

100 with ∼95% RH via regulating aerosol and sheath air flow (Maßling et al., 2003). The associated uncertainties with

101 RH measurement at 90% RH are 1.0%. The particle hygroscopic growth distribution at a specific humidity and

102 dry size (D$_p$, dry) can be conveniently determined through CPC. There are two humidity sensors (Vaisala) in the

103 system for aerosol flow and sheath flow respectively. The sensors in the second DMA were calibrated

104 automatically every 30 min at 90% RH using 100 nm ammonium sulfate ((NH$_4$)$_2$SO$_4$) particles to analyze stability

105 at high RH. The measurement error of the HTDMA depends mainly on RH measurement and control uncertainties

106 within the system (Su et al., 2010). All RH sensors were calibrated using the Vaisala salt kit containing LiCl,

107 NaCl, KCl and so forth, before the measurement campaign. Size calibration for both DMAs involved the

108 application of Latex particles of standard size, 200 nm prior to measurement. The number concentration peak

109 occurred at 203 nm, which attests to the accuracy of DMAs' size selection at 1.5%. The HTDMA system was

110 used to measure the hygroscopic growth factors (HGFs) of particles with D$_p$, dry of five different sizes (20, 50,

111 100, 150 and 200 nm), at 90% RH. The full scan covering all five sizes had a time resolution of approximately 30

112 minutes.

113 Particle number size distributions (PNSDs) and particle volume-size distributions (PVSDs) were measured using

114 a MPSS.

115

116
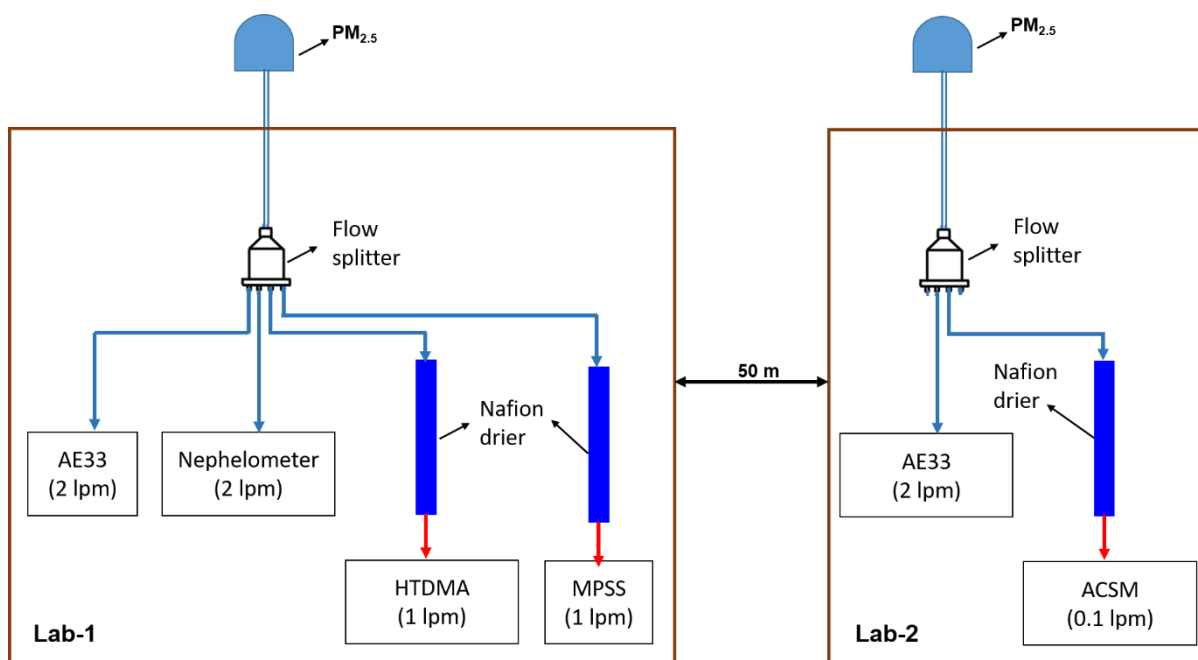
Figure 1: Schematic diagram of the inlet systems for aerosol sampling instruments. The blue and red sampling lines indicate the ambient air and dehumidified (RH<25%) ambient air, respectively.

2.2 Meteorological and Gas Data

The gas data was obtained from the R.K. Puram-DPCC monitoring station, a continuous ambient air quality monitoring station managed by the central control room for air quality management (Delhi-NCR). The data was downloaded from the CPCB website (https://app.cpcbccr.com/ccr/#/caaqm-dashboard/caaqm-landing/data). R.K. Puram is situated 3.5 km northwest of IIT Delhi. The automatic weather station (Watch Dog 2000 series) continuously measured wind speed (WS), wind direction (WD), temperature (T), and relative humidity (RH). The station is installed on the rooftop of the 9th-floor building at IITD.

2.3 Data Analysis

2.3.1 H-TDMA

Overall, we conducted 1483 cycles of HTDMA scans. After each cycle, we calculated the percentage difference between the measured and theoretical growth factors (Δq) for 100 nm ammonium sulfate particles. Only those cycles with $\Delta q \leq \pm 5\%$ were included for further data analysis, while the remaining cycles were discarded (Kecorius et al., 2019). As a result, we obtained 1102 HTDMA scan cycles that passed this data quality check. Regarding good scan cycles, we conducted 1449, 1431, 1438, 1470, and 1420 successful H-TDMA scans for particles of sizes 20, 50, 100, 150, and 200 nm particles, respectively, for further analysis. Subsequently, we

5

134 applied TDMAinv Toolkit, a piecewise linear TDMAinv algorithm developed by Gysel et al. (2009) and written

135 in IgorPro, to perform post-data processing on the raw HGF data. The measured distribution function is a

136 smoothed and skewed integral transformation of actual probability density functions for growth factors (GF-

137 PDFs). Gysel et al. (2009) provides a detailed account of the raw data processing in the TDMAinv toolkit for the

138 measurement of real HGFs. The TDMAinv toolkit was successfully employed in various studies across the globe

139 (Gysel et al., 2007; Liu et al., 2012; Sjogren et al., 2007; Wang et al., 2018a), including Kanpur, India (Mandariya

140 et al., 2020a). Furthermore, the RH in DMA2 generally reached the designated 90% value and remained stable

141 within ±1%. However, on occasion, it experienced significant drifts. To address this issue, all growth factors

142 measured between 88% and 92% RH were adjusted to the target value of 90% (HGF_90%) (Gysel et al., 2007)

143 with the kappa-model recommended in the TDMAinv toolkit (Gysel et al., 2009). This approach effectively

144 minimized the RH drifts in DMA2. After conducting scans at target RH for aerosol particles of 20, 50, 100, 150,

145 and 200 nm, 979, 957, 972, 969, and 966 of these scans were respectively corrected. The corrected scans were

146 then averaged for a 60-minute time resolution, resulting in 425, 429, 419, 424, and 417 scans.

147 Furthermore, using the kappa-Köhler theory (Mandariya et al., 2020a; Petters and Kreidenweis, 2007), we

148 calculated the size-resolved hygroscopicity factors (kappa, κ, say $\kappa_{\text{H-TDMA\_90\%}}$) from the corresponding size-

149 resolved target RH corrected HGFs, based on equation (1).

150 $$\kappa_{H-TDMA\_90\%} = (HGF\_90\%^3 - 1)\left[\frac{1}{RH} exp\left(\frac{4\sigma M_w}{RT\rho_w D_o HGF_{90}\%}\right) - 1\right], \tag{1}$$

151 Where, $\kappa_{\text{H-TDMA\_90\%}}$ represents the hygroscopicity factor at 90% RH, while HGF_90% is the size-resolve HGF at

152 90% RH. RH stands for atmospheric relative humidity expressed as a fraction, and σ denotes the surface tension

153 of the aerosol liquid droplet-air interface at the droplet surface measured in N/m, assumed to be nearly to pure

154 water. R represents the universal gas constant, expressed in units of J K^{-1} mol^{-1}. M_w denotes the molecular mass

155 of water while T signifies the ambient temperature in Kelvin (K). ρ_w signifies the density of water in kg/m^3. D_o

156 denotes the dry mobility diameter of the particle in meters (m).

2.3.2 MPSS

158 The electrical mobility distribution is measured by MPSS and then converted to PNSD in the 8 to approximately

159 800 nm mobility diameter range. This is achieved by utilizing an inversion algorithm to correct for multiple

160 charged aerosol particles (Wiedensohler, 1988; Pfieffer et al., 2014) and diffusional losses (Wiedensohler et al.,

161 2012; 2018).

162

163

2.3.3 ACSM

For a detailed account of the ACSM setup, please refer to Arub et al. (2020). The ACSM operated in a temperature-controlled laboratory at almost 0.1 lpm and 1-minute time resolution. It was set to measure mass-to-charge ratio (m/z) from 10 to 140. The PM_1 aerosol beam was concentrated and directed towards the vaporizer at 600 °C. The flash-vaporized compounds were then ionized through impact ionization at 70 eV electrons and detected using a quadrupole mass spectrometer (Ng et al., 2011). The study employed a 200 millisecond amu^{-1} scan speed and a pause setting of 125 for a sampling duration of 64 seconds to collect aerosol mass spectra using the ACSM technique. Refer to Gani et al. (2019) for comprehensive guidance on the ACSM operational procedures. For ACSM calibration and data processing, please refer to Patel et al. (2021). Positive matrix factorization (PMF) was conducted on the data, resulting in a four-factor solution: hydrocarbon-like OA (HOA), biomass burning OA (BBO), less-oxidized OA (LO-OOA), and more-oxidized OA (MO-OOA), as shown in Fig. S1. More information regarding PMF analysis can be found in section S.1 and Fig. S2 of the Supplementary information. Three different events were identified based on the temporal variation of mass concentration peaks of BBOA, HOA, and Cl (see Fig. 2): 1) a high-residential or biomass burning period (H-BB); 2) a high-hydrocarbon-like OA period (H-HOA); and 3) a high-chloride period (H-Cl). Additionally, the "Clean Period" was defined as a period where the PM_1 loading was less than the 25th percentiles (≤ 38.7 μg m^{-3}) for the sampling period. The event's starting and ending times were determined by the initial increase in concentration and subsequent return to the starting values as the concentration decreased.

2.3.4 Derived Secondary Inorganic Salts

The ACSM measures OA, NO_3, SO_4, NH_4, and Cl. A simplified ion-pairing scheme from Gysel et al. (2007) was adopted. However, NH_4Cl was not included in their ion-pairing scheme; therefore, we modified it to integrate ammonium chloride into the calculation. Thus, our modified ion-pairing scheme includes NH_4Cl (ACl), NH_4NO_3 (AN), $(NH_4)_2SO_4$ (AS), NH_4HSO_4 (ABS), and H_2SO_4 (SA) as shown below:

Case-1 $R_{SO_4}(NH_4 \ to \ SO_4) \leq 1$

$SA = 98.0795 \times \max\left(0, (n_S - n_A)\right)$

7

189     $ABS = 115.11 \times n_A$

190     $AS = 0$

191     $AN = 0$

192     $ACl = 0$

193   **Case-2 $1 < R_{SO_4} < 2$**

194     $SA = 0$

195     $ABS = 115.11 \times \left((2 \times n_S) - n_A \right)$

196     $AS = 132.1405 \times (n_S - n_A)$

197     $AN = 0$

198     $ACl = 0$

199   **Case-3 $R_{SO_4} \geq 2$**

200     $SA = 0$

201     $ABS = 0$

202     $AS = 132.1405 \times n_S$

203     $AN = \left(\min\left(\left(n_A - \left(\dfrac{ABS}{115.11}\right) - \left(\dfrac{(2 \times AS)}{132.1405}\right) \right), n_N \right) \right) \times 80.0434$

204     $ACl = \left(\min\left(n_C, \left(n_A - \left(\dfrac{ABS}{115.11}\right) - \left(\dfrac{2 \times AS}{132.1405}\right) - \left(\dfrac{AN}{80.0434}\right) \right) \right) \right) \times 53.54$

205   Here, "n" represents the number of moles, while "A", "N", "S", and "C" represents the species NH_4, NO_3, SO_4,

206   and Cl. Inorganic salts concentrations were also predicted using the NH_4, SO_4, NO_3, and Cl components of the

207   ISORROPIA v2.1 model. Our results shows a strong correlation and nearly unit slope (0.9999) between the

208   calculated and modeled inorganic salts, as presented in Fig. S3. This strongly justifies the new ion-pairing scheme

209   utilized in this study.

210   **2.3.5 Windrose and Potential Source Contribution Function (PSCF)**

211   The windrose plot was generated using the openair package in R (http://www.r-project.org, http://www.openair-

212   project.org). An offline based Hybrid Single-Particle Lagrangian Integrated Trajectory (HYSPLIT4) model

213   developed by NOAA/Air Resources Laboratory (ARL)) (Draxler and Hess, 1997) was used to estimate the 48-

214   hour back trajectory of air masses that reached DSL at 500 m above ground for the entire study period at hourly

215   intervals.. The meteorological data used for back trajectories was obtained from ARL's Global Data Assimilation

216   System archive, specifically the GDAS 0.5 degree archive (http://ready.arl. noaa.gov/archives.php). We used

217   these estimated back trajectories and the measured mass fraction of chemical species of bulk aerosol as input in

218   conducting Potential Source Contribution Function (PSCF) analysis. This analysis was carried out with the aid of

219   Zefir (version 3.7), a tool written in Igor Pro (WaveMetrics). The Zefir tool is described in detail elsewhere (Petit

220   et al., 2017). Additionally, this tool was used to create the box plots discussed in the following section. To calculate

221   the aerosol liquid water content (ALWC) as a function of inorganic species mass concentration, ambient T, and

222   RH, the ISORROPIA-II model (Fountoukis and Nenes, 2007) was utilized.

223   **3. Result and Discussions**

224   **3.1 Overview of meteorology, trace gases, and aerosol characterization**

225   Fig. 2 depicts the hourly-resolved temporal changes of various meteorological parameters, including RH, T, WD,

226   and WS, PNSD, PVSD, principal components of non-refractory PM_1, and OA with their corresponding fractional

227   mass contributions. In addition, Fig. S5 exhibits the temporal fluctuations of atmospheric gases, specifically

228   nitrogen oxides (NOx), carbon monoxide (CO), and sulfur dioxide (SO_2). Delhi's winter climate is mainly affected

229   by a depression caused by Western Disturbances, resulting in cold waves in the region. The ambient RH and T

230   vary within the range of 24.2% to 96.6% and 9.0 °C to 28.5 °C, respectively. The average values of RH and T are

231   56.0% ± 18.2% and 18.7 °C ± 4.2 °C, respectively. These fluctuations indicate a shift in Delhi's atmosphere

232   transitions from being damp and chilly in February to dry and relatively warm in March. Nighttime conditions are

233   consistently cooler and more humid than daytime conditions throughout the sampling period. Ambient RH

234   exhibits a diurnal pattern, with a peak occurring during the early morning hours (06:00-07:00) and a valley

235   appearing around midday (13:00-15:00). Conversely, ambient temperature follows an opposing trend, increasing

236   at midday, which can be correlated with higher solar radiation during those hours (refer to Fig. 3a & b). The high

237 ambient temperature and peak O_3 concentration observed during midday (see Fig. 3(i)) indicate the possibility of

238 daytime photo-oxidation processes according to research carried out by Nelson et al. (2023). Fig. S6 displays the

239 variation of WS and WD, ranging from 0.0 to 5.6 (with an average of 1.0 ± 1.0) m/s and 4.0 to 345.7 (with an

240 average of 197.1 ± 84.4) degrees from the North, respectively. The majority of wind directions were in the WNW-

241 WSW and E-ESE direction. These patterns indicate that the air quality in Delhi remained relatively stagnant

242 throughout the study period. The measured aerosols are likely to be a result of local emissions and aerosol

243 chemistry.

244 Throughout the sampling period, ambient trace gases NOx and CO demonstrate notable variability, peaking from

245 local burning activities. During intense biomass burning activities, ambient NOx levels reach a maximum of 421.2

246 ppb (58.4 ± 61.9). CO concentrations also reach maximum levels during similar periods as NOx, varying from

247 0.0 to 7.66 ppm (0.58 ± 0.79), as illustrated in Fig. S5. The time-specific changes in the levels of these trace gases

248 are illustrated in Fig. 3 (f, g, h, and i). The graph indicates two crests (06:00-08:00 and 17:00-20:00 hours), which

249 are attributed to local biomass/trash burning emissions that happen in the morning and heavy traffic during

250 nighttime rush hours. Conversely, SO_2 demonstrates a distinct pattern, with varying concentrations ranging from

251 0.46 to 9.55 ppb (4.41 ± 1.20). Notably, it exhibits peaks during the morning (09:00-12:00 hours) and at midnight

252 (21:00-02:00 hours), which are connected to local industrial stack emissions.

253 The PM_1 particle number concentration ranges from 408 to 29,845 particles/cm^3 (11319 ± 5552). Elevated particle

254 number concentrations are commonly linked to local burning incidents. The particle concentration sees a rise in

255 the evening (at 06:00 PM) and peaks at midnight, implying an increase in residential burning activity and traffic

256 exhaust emissions. These activities likely contribute to the decrease in the geometric mean diameter (GMD) of

257 the PNSD, which is around 47 nm. However, this value increases to nearly 87 nm, as shown in Fig. 3(t), indicating

258 the organic aerosol's nighttime aging. Fig. 3(y) depicts that the hourly averaged mean diurnal GMD of PVSD

259 varies from about 274 to 324 nm, with a mean value of 309.1 ± 33.1 nm. This average is similar to the higher-end

260 particle size of 200 nm hygroscopicity measurement used in this study. Therefore, the ACSM bulk aerosol

261 composition is the most appropriate option for discussing the hygroscopicity of these particles.

262 The PM_1 concentration, also known as hourly time-resolved NR-PM_1, ranged from 9.0 to 357.9 µg/m^3 with an

263 average of 81.2 ± 56.6 µg/m^3. This range is consistent with the 12.7-392 µg/m^3 (NR-PM_1) boundary previously

264 reported by Gani et al. (2019) at the same sampling location. Prakash et al. (2018) found that PM_1 mass

265 concentration accounts for 83% of $PM_{2.5}$, indicating the prevalence of combustion-based particles. Additionally,

266 we observed a high correlation ($r^2 = 0.83$, p<0.05) between PM_1 measured by ACSM and MPSS, assuming an

267 effective aerosol density of 1.6 g/cm^3 (refer to Fig. S4). The OA ranged from 1 and 293 (46.5 ± 39.6) µg/m^3, with

268 PM_1 being the predominant fraction. These findings are consistent with the range of 53.3 to 166 (112) µg/m^3

269 observed during the winter months (December-February) at the same location (Gani et al., 2019). However, the

270 decrease in average OA concentration during the measuring period of February-March can be explained by the

271 reduction in aerosol loading after its peak in December-January (Gupta and Mandariya, 2013). The campaign

272 average fractional contribution of OA to PM_1 was 56%, with a range of 1 to 84%. This high OA concentration in

273 fine particulate matter (PM_1) aligns with findings from prior studies in the IGP, including those conducted by

274 Chakraborty et al. (2016a), Gani et al. (2019), and Mandariya et al. (2019), as well as those conducted worldwide,

275 such as by Jimenez et al. (2009) and Zhang et al. (2007). Peak OA mass concentrations were observed between

276 9:00 PM and 11:00 PM (figure 2(k)), which is in line with observations made at the same site by Gani et al. (2019)

277 and Rai et al. (2020). The average mass concentration of NO_3 during the campaign was 10.1 ± 7.0 µg/m^3,

278 exhibiting diurnal variation with distinct peaks in the morning and at midnight (Fig. 3(l)). Additionally, SO_4

279 demonstrated a slight enhancement at 08:00 hr, and its concentration remained relatively stable from noon to

280 17:00 hr (Fig. 3(m)). Conversely, Cl experienced significant fluctuations, ranging from 0.13 to 77.83 µg/m^3, with

281 higher concentrations of Cl occurring episodically throughout the campaign. The Cl concentration aligns with

282 Gani et al. (2019)'s previously reported value of 0.1-66.6 µg/m^3 at the same location. Fig. 2(g and h) illustrates

283 the temporal variation of various OA factors. The mass concentration of BBOA peaks during the nighttime and

284 morning hours (Fig. 3(r)). On the other hand, LO-OOA exhibits a peak in the morning and remains relatively

285 stable at noontime, indicating a steady formation. Meanwhile, MO-OOA exhibited a slight rise around midday,

286 suggesting daytime photooxidation formation (Mandariya et al., 2019; Sun et al., 2016). During the sampling

287 period, oxygenated organic aerosol (OOA) comprised the majority of OA. The BBOA mass concentration during

288 H-BB events varied dynamically, ranging from 16.3 to 134.7 µg/m^3, with an average of 50.7 ± 24.0 µg/m^3.

289 Concurrently, these events displayed higher levels of HOA, ranging from 9.6 to 109.4 µg/m^3, indicating a likely

290 similarity in the sources of HOA during this particular incident. However, during H-HOA events, concentration

291 of HOA were higher, ranging from 4.8 to 58.9 µg/m^3, although these amounts were notably lower than those

292 observed during H-BB events. Nonetheless, the fractional mass contribution of HOA to OA was the largest of all

293 OA categories. Additionally, during H-Cl events, there were increased concentrations of both primary organic

294 aerosol HOA and BBOA. BBOA made up about 40.0%, 21.1%, 32.5%, and 13.1% to OA during H-BB, H-HOA,

295 H-Cl, and relatively clean events, respectively, indicating varied sources of BBOA. Furthermore, the average

contribution of H-HOA was the highest during the H-HOA event, at 41.6%. During the H-Cl event, Cl's

contribution to the fractional mass in PM_1 peaked up to 44.9%, which was higher than the contributions of 21.2%

in H-BB events and 7.3% in H-HOA events.
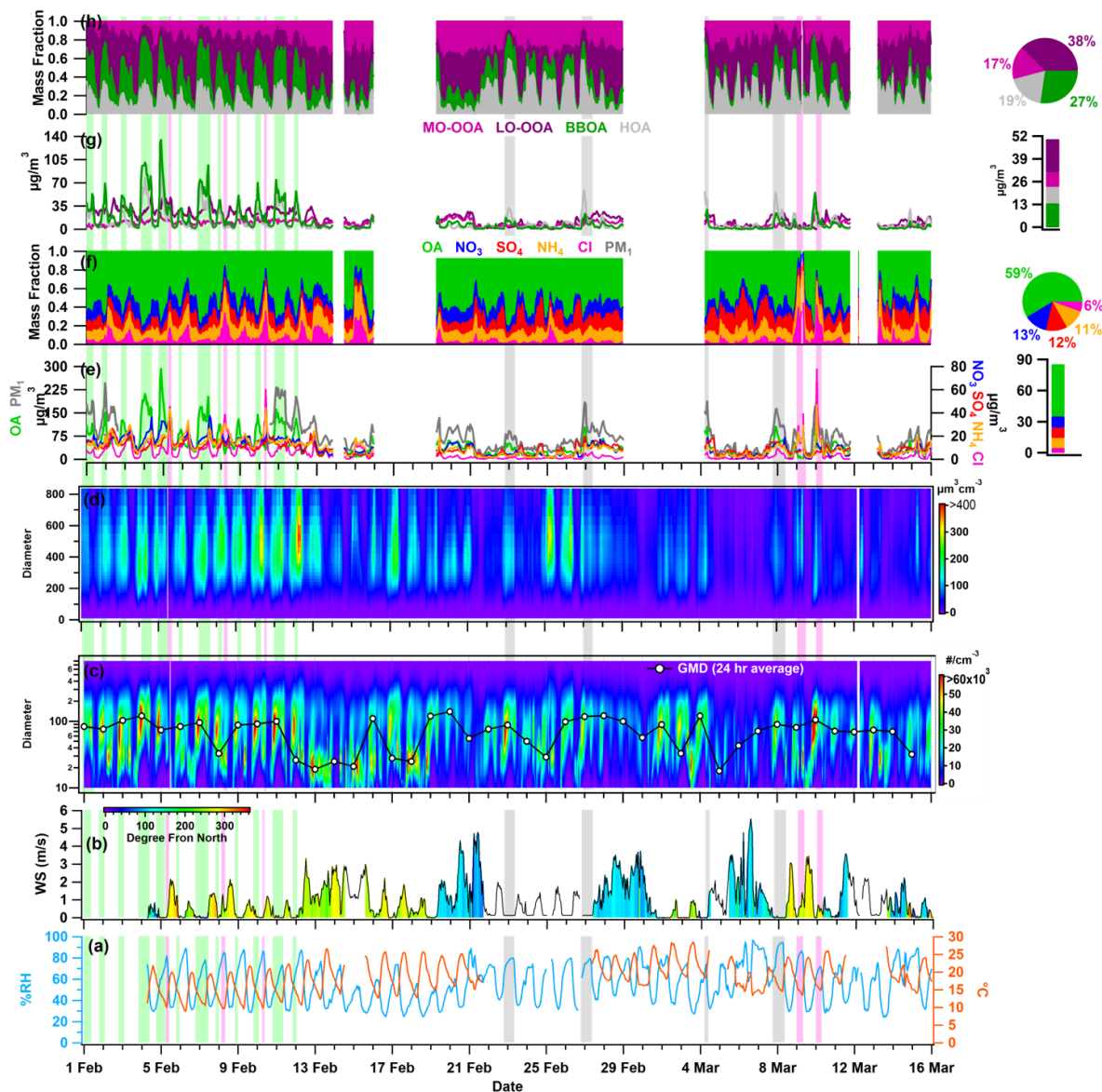
Figure 2: Temporal variability of ambient (a) relative humidity (RH), temperature (T), (b) wind speed (WS), wind direction (WD), (c) particle number-size distribution (PNSD), 24-average geometric mean diameter (GMD), (d) particle volume-size distribution (PVSD), (e) particulate matter (PM_1), organic aerosol (OA), nitrate (NO_3), sulfate (SO_4), ammonium (NH_4), chloride (Cl), (f) fractional contribution of OA, NO_3, SO_4, NH_4, and Cl in PM_1, (g) more oxidized-oxygenated OA (MO-OOA), less oxidized-oxygenated OA (LO-OOA), biomass burning OA (BBOA), hydrocarbon like-OA (HOA), and (h) fractional contribution of MO-OOA, LO-OOA, BBOA, and HOA in OA. The pie chart sub-plot represents the overall average contribution of species, and the bar sub-plot represents the overall campaign average

12

value of different species. All other species are represented with specific color coding mentioned in legends. The light green, grey, and pink color shaded vertical line indicates the high-BBOA (H-BB), high-HOA (H-HOA), and high-Cl (H-Cl) events, respectively. The discontinuity in the data points marks the missing data or non-sampling time.
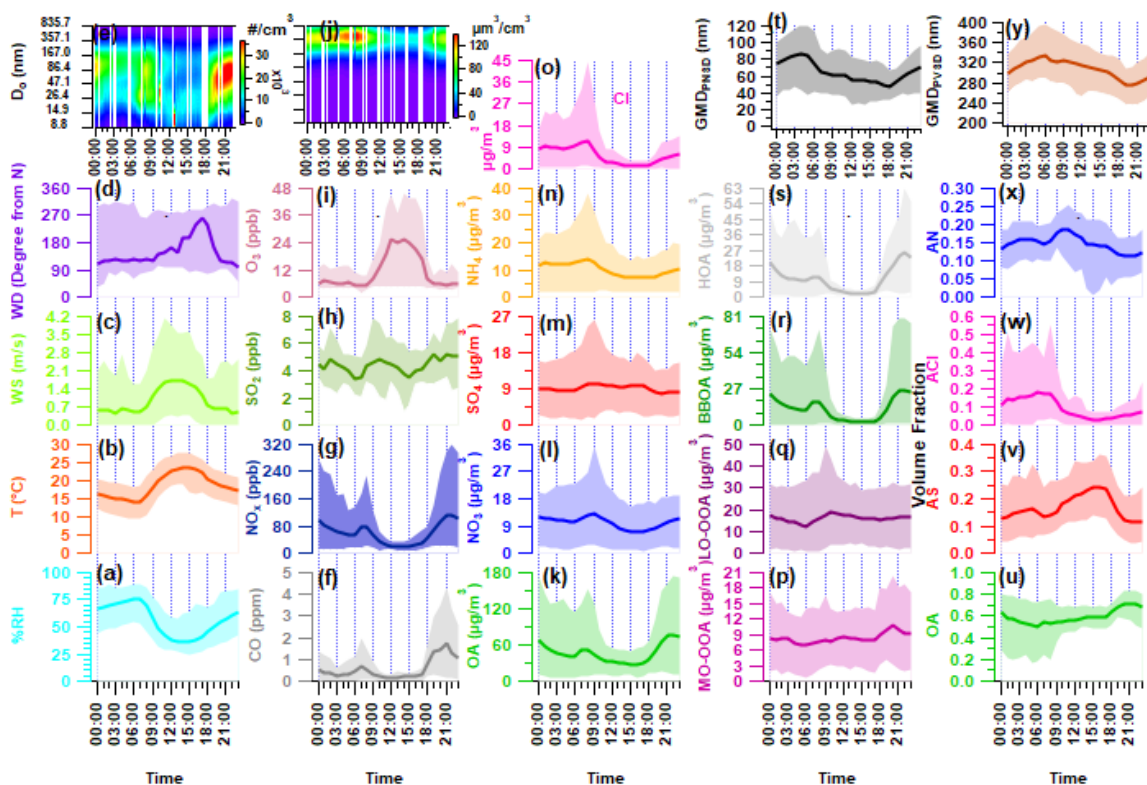
Figure 3: Diurnal variation of ambient meteorological parameters (a) % ambient relative humidity (RH), (b) temperature (T), (c) wind speed (WS), (d) wind direction (WD), and (e) particle number size distribution (PNSD), mass concentration of ambient trace gases (f) carbon mono-oxide (CO), (g) nitrogen oxides (NOx), (h) sulfur dioxide (SO₂), and (i) ozone (O₃), (j) particle volume size distribution (PVSD), mass concentration of aerosol constituents (k) organic aerosol (OA), (l) nitrate (NO₃), (m) sulfate (SO₄), (n) ammonia (NH₄), and (o) chloride (Cl), mass concentration of organic aerosol species (p) more oxidized-oxygenated OA (MO-OOA), (q) less oxidized-oxygenated OA (LO-OOA), (r) biomass burning OA (BBOA), and (s) hydrocarbon like-OA (HOA), (t) geometric mean diameter of particle number size distribution (GMD$_{PNSD}$) and volume fractional contribution of (u) organic aerosol (OA), (v) ammonium sulfate (AS), (w) ammonium chloride (ACl), and (x) ammonium nitrate (AN) in PM₁, and (y) geometric mean diameter of particle volume size distribution (GMD$_{PVSD}$). Upper and lower boundary of shaded area represents the 95th and 5th percentile values of respective species.
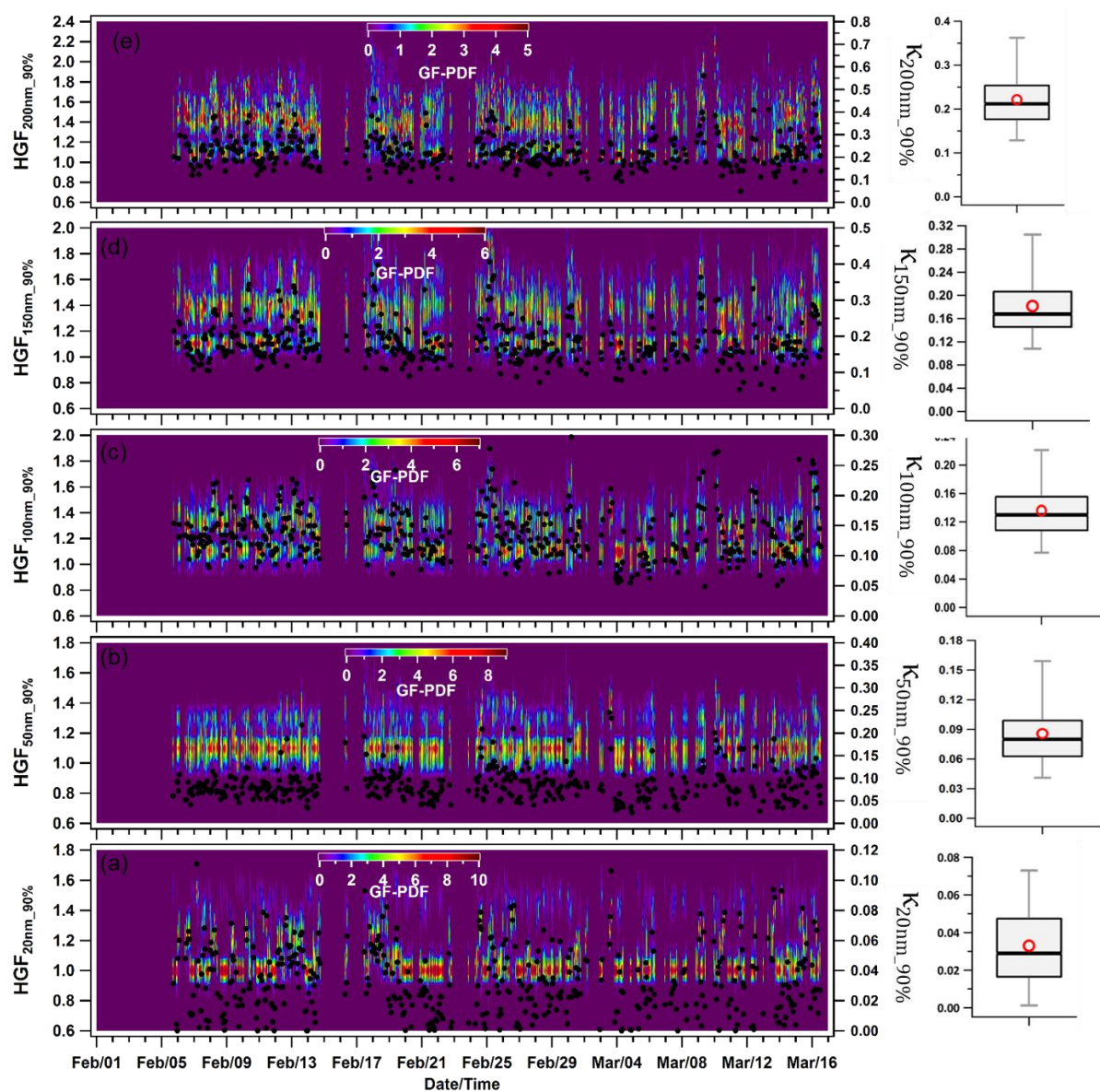
3.2 Hygroscopicity of Nucleation, Aitken, and Accumulation Mode Particles

3.2.1 Temporal variability

325 Fig. 4 displays the hourly averaged dynamic variability of $HGF_{90\%}$ and $\kappa_{H\text{-}TDMA\_90\%}$ (kappa) for aerosol particles

326 in the Nucleation, Aitken, and Accumulation modes at 90% ambient relative humidity. The hygroscopic growth

327 factors of particles sized at 20 ($HGF_{90\%\_20nm}$), 50 ($HGF_{90\%\_50nm}$), 100 ($HGF_{90\%\_100nm}$), 150 ($HGF_{90\%\_150nm}$), and 200

328 nm ($HGF_{90\%\_200nm}$) varied between 1.00-1.41, 1.05-1.39, 1.11-1.49, 1.12-1.63, and 1.12-1.79. The averaged

329 hygroscopic growth factors of the 20, 50, 100, 150, and 200 nm aerosol particles were 1.14 ± 0.09 (average $\pm$

330 standard deviation), 1.16 ± 0.06, 1.27 ± 0.07, 1.35 ± 0.09, and 1.41 ± 0.09, respectively. These values indicate

331 statistical significance ($p<0.05$) between the different hygroscopic growth factors. Moreover, the hygroscopicity

332 values ($\kappa_{20nm\_90\%}$ and $\kappa_{50nm\_90\%}$) of the aerosol particles were found to range between 0.00-0.11 and 0.02-0.25 for

333 the 20 nm and 50 nm particle sizes, respectively, with an average of 0.03 ± 0.02 and 0.09 ± 0.03. Nucleation mode

334 particles, consisting mainly of monomodal GF-PDF (Fig. 4(a)), consisted of approximately $74 \pm 24\%$ nearly

335 hydrophobic particles (HGF <1.2). However, this percentage increased to 100% and was associated with

336 nighttime local burning activities, as demonstrated in Fig. 4(a). The nucleation mode particles ($\kappa_{20nm\_90\%}$) exhibited

337 significantly ($p<0.05$) lower hygroscopicity than the Aitken mode particles ($\kappa_{50nm\_90\%}$). Hong et al. (2015) found

338 that nucleation mode particles have higher susceptibility to condensable vapors such as newly-emitted VOCs,

339 H_2SO_4 and HCl. Nevertheless, the study at hand did not measure these substances. The κ value of Aitken-sized

340 particles was comparable to the 0.24 ± 0.08 of 52.6 ± 6.9 size particles reported by Gunthe et al. (2011) for Beijing,

341 like Delhi, is one of the most polluted urban area. Gunthe et al. (2011) conducted this study on CCN at

342 supersaturation levels, justifying the comparison. The campaign average hygroscopicity parameter (kappa, $\kappa_{90\%}$)

343 increased significantly ($p<0.05$) with particle size, attributed to the Kelvin effect (Wang et al., 2018a). In the

344 accumulation size range of 100, 150, and 200 nm, $\kappa_{90\%}$ increased to approximately 0.56. The mean values for

345 $\kappa_{100nm\_90\%}$, $\kappa_{150nm\_90\%}$, and $\kappa_{200nm\_90\%}$ were 0.14 ± 0.04, 0.18 ± 0.06, and 0.22 ± 0.07, respectively. The range for

346 $\kappa_{200nm\_90\%}$ was between 0.05 and 0.56. Similar variations of κ with particle size have been observed globally

347 (Cerully et al., 2015; Enroth et al., 2018; Fan et al., 2020; Kawana et al., 2016; Kim et al., 2020; Kitamori et al.,

348 2009; Ogawa et al., 2016; Sjogren et al., 2012; Wang et al., 2018a), including in Kanpur, India, situated in the

349 center of the IGP (Mandariya et al., 2020a). These variations have been attributed to the prevalent increase in

350 inorganic to organic aerosol fraction in particles with size increment. Furthermore, Arub et al. (2020) reported

351 that $\kappa_{H\text{-}TDMA\_90\%}$ was approximately in the range of 0.13-0.77 for PM_1 in Delhi, without considering BC. However,

352 their theoretical prediction of particles' hygroscopicity took into account a particle's chemical composition,

353 leading to more precise results. Arub et al. (2020) thus provided a theoretical prediction of particles'

hygroscopicity by considering a particle's chemical composition. A 10% in κ calculation was observed when considering BC in the aerosol chemical composition. Additionally, the $\kappa_{\text{H-TDMA\_90\%}}$ measured in this study aligned with the global average value of 0.27 ± 0.21 for continental aerosols (Petters and Kreidenweis, 2007; Pringle et al., 2010). Subsequent sections will discuss the impact of a particle's chemical composition, local meteorology, and air mass trajectories on $\kappa_{\text{H-TDMA\_90\%}}$ for accumulation mode particles.

Figure 4: Temporal variability in hygroscopicity parameter kappa (κ) of nucleation mode particles (a) 20 nm ($\kappa_{20nm\_90\%}$), Aitken mode particles (b) 50 nm ($\kappa_{50nm\_90\%}$), and Accumulation mode particles (c) 100 nm ($\kappa_{100nm\_90\%}$), (d) 150 nm ($\kappa_{150nm\_90\%}$), and (e) 200 nm ($\kappa_{200nm\_90\%}$). The box plots represent the variability in the hygroscopicity of

15

364 respective sizes of particles in which low and high whisker traces represent the 5 and 95 percentile, respectively. The

365 red marker indicates the average of the data, whereas the upper and lower sides of the boxes indicate the 75 and 25

366 percentile of the data, respectively.

367 **3.2.2 Diurnal variability**

368 The diurnal variation in $\kappa_{\text{H-TDMA\_90\%}}$ differed for nucleation ($\kappa_{20\text{nm\_90\%}}$), Aitken ($\kappa_{50\text{nm\_90\%}}$), and Accumulation

369 ($\kappa_{100\text{nm\_90\%}}$, $\kappa_{150\text{nm\_90\%}}$, and $\kappa_{200\text{nm\_90\%}}$) mode particles. Fig. 5 illustrates the hourly-resolved average κ for each

370 particle size, showing a diel trend. The larger particles displayed higher κ values than the smaller ones, consistent

371 with trends observed in Kanpur, India (Mandariya et al., 2020a) and other locations worldwide (Fan et al., 2020;

372 Hong et al., 2015). Overall, all particle sizes exhibited a "late-night hump" (02:00-05:00 hr) in $\kappa_{\text{H-TDMA\_90\%}}$. Only

373 $\kappa_{20\text{nm\_90\%}}$ displayed a diurnal variation with two peaks: one occurring late at night (02:00-04:00 hr) and the other

374 at noon (14:00-16:00 hr). Additionally, two valleys were observed during the morning (07:00-10:00 hr) and night

375 (19:00-22:00 hr), which indicate the strong influence of local burning and traffic activities (Pringle et al., 2010).

376 Furthermore, nucleation-sized particles were potentially contributed by nearly hydrophobic particles (HGF<1.2)

377 from evening to midnight. Mono-modal GF-PDF was exhibited around a unit hygroscopic growth factor,

378 potentially suggesting the presence of locally-emitted particles. The 20 nm particles are of sufficient small size to

379 be classified as nucleation mode particles. Similar diurnal trends of Nucleation and Aitken mode particles have

380 been observed by Achtert et al. (2009), who attributed the lower values to the emission of hydrophobic aerosol

381 particles during the local burning emissions. The daytime hump in aerosol particle composition can be attributed

382 to the intensity of the photochemical oxidation process, resulting in the amplification of more oxidized species.

383 Moreover, the gaseous condensation of H_2SO_4, HNO_3, and VOCs predominantly controls their chemical makeup

384 (Hong et al., 2015). The variability of $\kappa_{\text{H-TDMA\_90\%}}$ can be addressed by taking into account the chemical

385 composition of the aerosol. Although $\kappa_{50\text{nm\_90\%}}$ exhibited less variation, it follows a diurnal pattern similar to

386 $\kappa_{20\text{nm\_90\%}}$. Furthermore, when the dry size of the aerosol particles increased to the accumulated mode, the diurnal

387 variation shifted towards nearly constant for the rest of the day. Hong et al. (2018) found no discernible diurnal

388 variation of 100- and 150-nm particles of organic-dominated aerosols in China's Pearl River Delta region.

389 Furthermore, the diurnal cycles of aerosol physicochemical properties also reflect the dynamic diurnal variation

390 in the planetary boundary layer (PBL), leading to particle accumulation during the night. The study only addressed

391 trend variability using bulk-aerosol composition, as size-resolved chemical composition was not quantified.

392 However, the daily average aerosol PNSD ranged from 18.0-140.0 nm, with a mean of 73.1 ± 33.8 nm. The shift

393 in PVSD mode occurred in the 300-600 nm. Range, making it appropriate to analyze the $\kappa_{200nm\_90\%}$ variation in

394 association with the bulk chemical properties of aerosols. Fan et al. (2020) demonstrated in Fig. 3 (r, s t, u, and v)

395 that the increase in the ratio of inorganic volume fraction to OA volume fractions is responsible for the peak in

396 hygroscopicity observed in the early morning hours. Additionally, in the winter during mid-night and early

397 morning, water-soluble organic and inorganic gases undergo partitioning and/or coagulation/condensation on the

398 surface of pre-existing particles. Furthermore, at high RH and lower temperatures, primary and secondary, less-

399 oxidized organic aerosols engage in the aging process. This leads to improved oxidation through

400 aqueous/heterogeneous reactions, thereby increasing the hygroscopicity of the particles (Jimenez et al., 2009; Wu

401 et al., 2016). Similar findings were reported by Fan et al. (2020) for winter in urban Beijing. They have attributed

402 this to the increase in hygroscopic particles due to the aqueous-oxidation and/or condensation process on the pre-

403 existing particles. Generally, stronger noontime solar radiation promotes more intense photooxidation processes.

404 The process promotes the distribution of fairly more oxidized and less volatile organics on the surface of particles,

405 thus augmenting the hygroscopic nature of particles that belong to the accumulation mode (Duplissy et al., 2011;

406 Massoli et al., 2010; Tritscher et al., 2011). The $\kappa_{H\text{-}TDMA\_90\%}$ exhibited a noontime flattening pattern, which was

407 due to a combination of the positive and negative effects resulting from an increase in the volume fraction of OA

408 and more hygroscopic ammonium sulfate and a decrease in ACl, and AN's volume fraction. A potential factor

409 that modulates the hygroscopicity of accumulation mode particles is the lower volume fraction contribution of

410 highly volatile ACl. This correlation is strongly supported by the $\kappa_{H\text{-}TDMA\_90\%}$ and the volume fraction of ACl (ε_{ACl})

411 in the corresponding size particles.
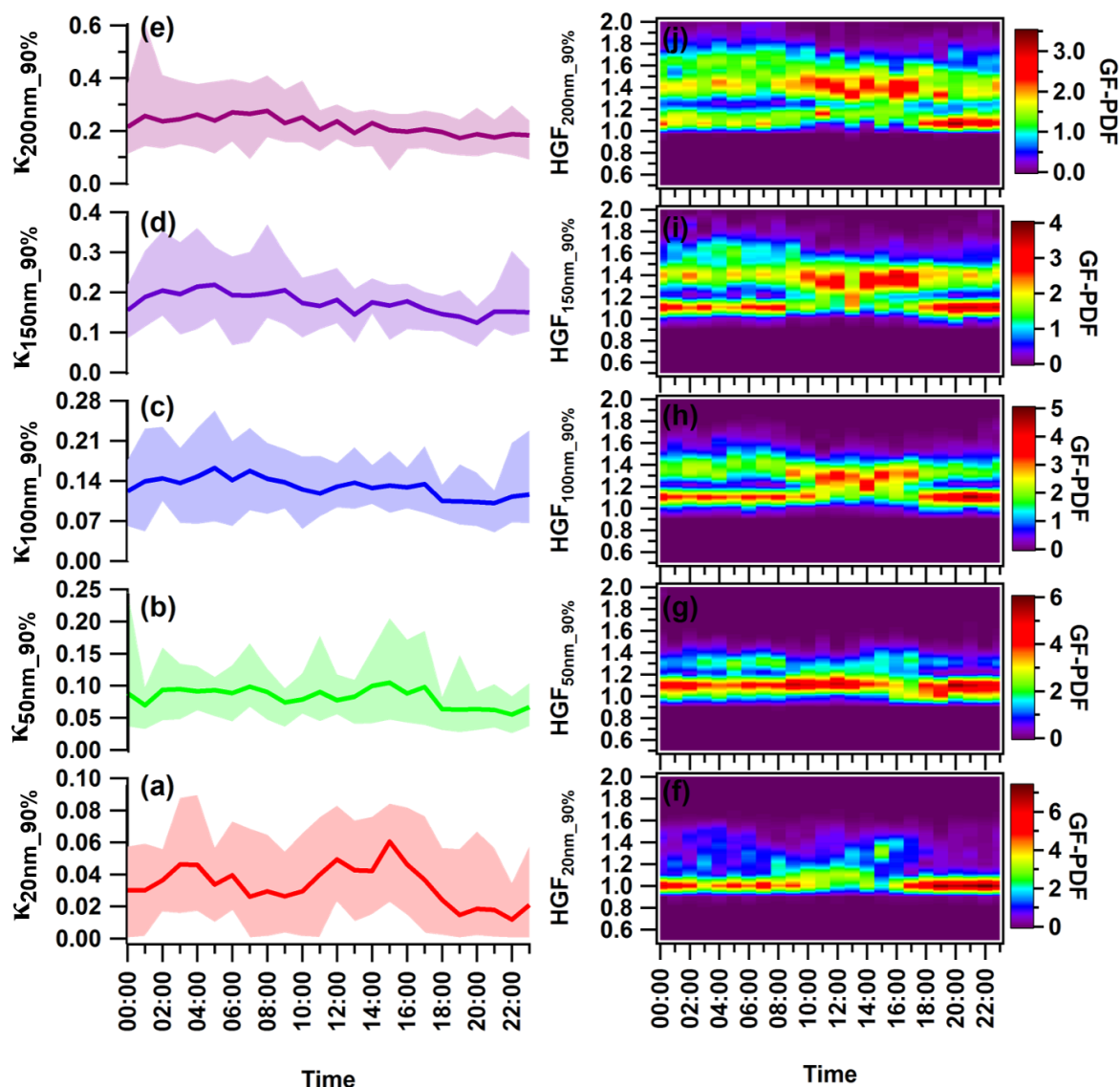
Figure 5: Diurnal variance in the hygroscopic parameter kappa (κ) of nucleation mode particles (a) 20 nm ($\kappa_{20nm\_90\%}$), Aitken mode particles (b) 50 nm ($\kappa_{50nm\_90\%}$), and Accumulation mode particles (c) 100 nm ($\kappa_{100nm\_90\%}$), (d) 150 nm ($\kappa_{150nm\_90\%}$), and (e) 200 nm ($\kappa_{200nm\_90\%}$) and hygroscopic growth factor of (f) 20 nm (HGF$_{20nm\_90\%}$), (g) 50 nm (HGF$_{50nm\_90\%}$), (h) 100 nm (HGF$_{200nm\_90\%}$), (i) 150 nm (HGF$_{150nm\_90\%}$), and 200 nm ($\kappa_{200nm\_90\%}$) aerosol particles. The solid line represents diurnal average values, and the upper and lower shaded area represents 95 and 5 percentile values of corresponding average values. Different color coding has been used to represent various size-specific kappa values. The color scale represents the growth factor probability density function of hygroscopic growth factor.

3.2.3 Driving Factor of Hygroscopicity

A correlation analysis was conducted between the measured chemical species and aerosol hygroscopicity to investigate the factors governing aerosol hygroscopicity, as presented in Fig. 6. It was found that organic aerosol

18

423   negatively affected κ, as evidenced by a negative correlation (Fig. S7(a)). The negative correlation between OA

424   and κ has been noted in India (Bhattu et al., 2016; Mandariya et al., 2020b) and globally (Enroth et al., 2018;

425   Hong et al., 2014; Kawana et al., 2016; Kitamori et al., 2009; Wang et al., 2018a; Wu et al., 2013a). These findings

426   suggest that primary constituents were predominant during high loading and may have been nearly hydrophobic

427   or less hygroscopic. The present study found that a 10% increase in volume of OA in 200 nm aerosol particles led

428   to a 4% reduction in their ability to attract water (hygroscopicity) (Fig. S7(a)). It is noteworthy that ammonium

429   sulfate and nitrate exhibited a weak positive correlation with hygroscopicity (Fig. 7(b and c)). This may be

430   attributed to sulfate and nitrate aerosols dominant in larger particles (>200nm). However, an increase in AS

431   volume by 10% was found to be responsible for a mere 1.6% increase in hygroscopicity. If the aerosol composition

432   had an increased AS contribution, the water-bound capacity of the aerosol was negatively affected (refer to Fig.

433   S8b). Additionally, as shown in Fig. 6(a), there was an increase in the volume fraction of ACl in PM_1 with an

434   increase in aerosol hygroscopicity. This strong positive correlation was responsible for a 4.2% increase in kappa

435   over the increment of 10% ACl by volume. This was the highest among all chemical species. Furthermore,

436   ammonium chloride has a greater capacity for water absorption (Chen et al., 2022; Zhao et al., 2020), which is

437   supported by the strong correlation between ALWC and the mass fraction of ACl in PM_1 as demonstrated in Fig.

438   6(b). The increasing fraction of ACl in PM_1 may therefore be attributed to the higher water uptake potential of

439   ammonium chloride. This implies that particles with a higher proportion of ammonium chloride absorb more

440   water vapor, resulting in larger hygroscopic aerosol particles. It is evident that the rise in ammonium chloride

441   proportion amplifies aerosol liquid water content, resulting in greater aerosol particle hygroscopicity. A recent

442   study conducted in Delhi by Chen et al. (2022) revealed that the fraction of ammonium chloride in PM_1 aerosol

443   increases significantly during higher relative humidity conditions in the winter season. This is due to the co-

444   condensation of semivolatile ammonium chloride with water vapor on particles, leading to enhanced water uptake

445   and severe winter haze in Delhi. The high volume fractions (over 30%) of ACl in atmospheric PM_1 were observed

446   sporadically, leading to the conclusion that the high chloride fraction in the particle phase heavily relies on excess

447   ammonia in the atmosphere. These findings suggest that ammonia plays a crucial role in determining chloride

448   partitioning in the particle phase, leading to increased aerosol water content in high relative humidity conditions

449   and lower temperature. The concentration of ACl relies heavily on both RH and temperature.
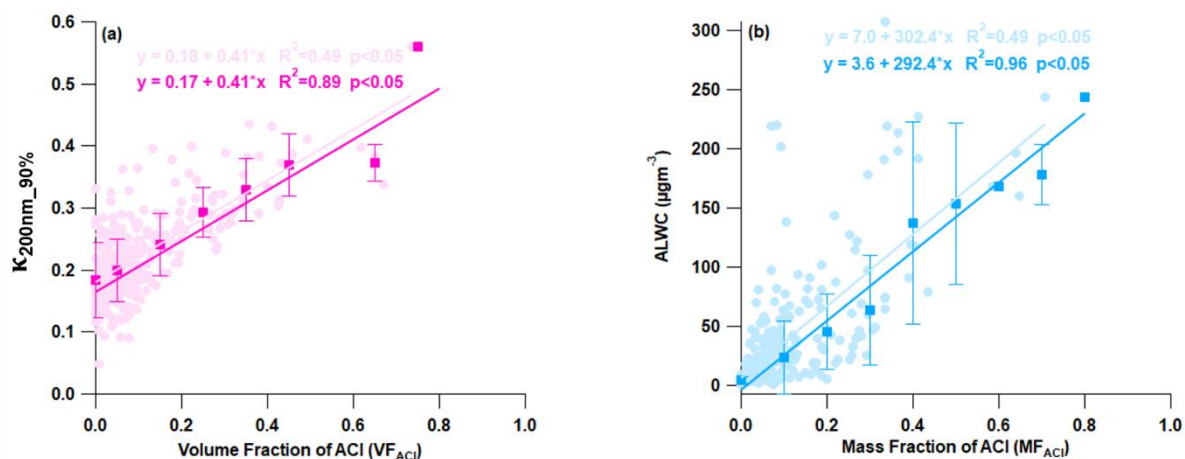
Figure 6: Correlation plot for (a) $\kappa_{200nm\_90\%}$ vs volume fraction of ammonium chloride aerosol (VF_{ACl}) and (b) aerosol liquid water content (ALWC) vs mass fraction of ammonium chloride (MF_{ACl}). The solid circle and square marker represent the individual data points and the average of 10% volume and mass fraction increment of ACl data points, respectively. The light and dark color regression lines and equations indicate the overall and average (10% volume and mass fraction increment) correlation, respectively. The error bars indicate the standard deviation of the data points within the 10% mass and volume fractional bins.

3.2.4 Hygroscopicity during high biomass burning (H-BB), high-hydrocarbon like OA (H-HOA), high-Cl (H-Cl), and relatively clean periods

Delhi's atmosphere is a complex mixture of chloride and organic aerosol sources resulting from combustion (including crop residue, agriculture waste, medical waste, municipal waste, plastic, etc.) and industrial activity. To examine the influence of chloride and OA on aerosol hygroscopicity, all episodic events were categorized into three groups. The first group was H-BB events, the second group was H-HOA events, and the third group was H-Cl events. Aerosol chemical composition data was filtered based on hygroscopic parameter data for subsequent analysis. This facilitates the retrieval of data specific to local emissions and atmospheric chemistry, as well as the effects of various potential transported air masses. Extracting any conceivable information pertaining to aerosol sources and transformation processes is valuable in interpreting their impact on aerosol hygroscopicity.

3.2.4.1 High-Cl (H-Cl) events

H-Cl events were selected as they correspond to a significant increase ($>20\%$) in the fractional volume contribution of NH_4Cl (ε_{ACl}) in the PM_1 aerosol at the receptor site. During this period, the surface wind mainly came from the west, although it was also influenced by wind from the west-northwest, west-southwest, and southeast, as illustrated in Fig. 7b. The average geometric mean diameter of the PNSD was almost 64 nm,

472 indicating that nearby fresh emission sources impact the particles. In addition, the average concentration of SO_2,

473 NOx, and CO concentrations were at 3.6 ppb, 51.9 ppb, and 0.4 ppm, respectively. The potential contributors to

474 BBOA and HOA were from the WNW and SE directions, as demonstrated in the bipolar plot Fig. 7(c & d), and

475 appeared to originate from a local source. Among the inorganic species, ACl displayed a strong correlation with

476 ambient RH, as illustrated in Fig. 7e and f, suggesting that atmospheric gaseous HCl was neutralized by NH_3 gas

477 in the presence of atmospheric water content. HCl sources may include coal power plants, solid waste dumping

478 sites with burning trash, and industries in the W-WSW direction (Gani et al., 2019), as depicted in in Fig. 7a.

479 Trash burning in Delhi during winter may potentially dominate atmospheric high Cl events (Shukla et al., 2021;

480 Tobler et al., 2020). In addition, the bipolar plots (Fig. 6(e and f)) indicate that ACl formation occurs under high

481 relative humidity conditions associated with a relatively calm atmosphere, thereby triggering particles

482 hygroscopicity. This hypothesis is supported by the strong correlation between ALWC, as discussed in the

483 previous section. Moreover, as shown in Fig. 8d, the GF-PDF of particles of all sizes shows a relatively higher

484 fraction of secondary mode particles contributing. More hygroscopic particles ($HGF_{90\%}>1.2$) accounted for higher

485 percentage of 42%, 47%, 50%, 74%, and 83% in particles ranging from 20nm to 200nm in size, respectively.

486 Therefore, ACl plays a significant role in increasing aerosol hygroscopicity, leading to the formation of fog/haze

487 under higher RH and colder atmospheric conditions.

488 Gunthe et al. (2021) observed that high local emissions of hydrochloric acid in Delhi during February-March are

489 partitioned into aerosol liquid water under high humidity conditions. This enhances the water uptake capacity of

490 aerosols, sustaining particle hygroscopic growth and resulting in fog/haze formation. Additionally, studies

491 worldwide on size-resolved hygroscopicity have observed Cl to be less than 1%, leading to the omission of ACl

492 as an aerosol constituent in the discussion. The current study did not find a strong correlation between κ with AS

493 or AN, which may be due to their association with larger particle sizes. Additionally, ACl may be associated with

494 particles of a comparatively smaller size (≤ 200 nm). Furthermore, in the context of examining the influence of

495 air mass trajectories, we mapped the constituents of aerosols in association with air mass back trajectories using

496 PSCF to determine the potential area source contribution that may be influencing the aerosol evaluation processes,

497 specifically the aerosol's hygroscopicity. However, we did not find any back trajectories that influenced the

498 receptor site, as all trajectory endpoints were observed above the height of the planetary boundary layer.

499
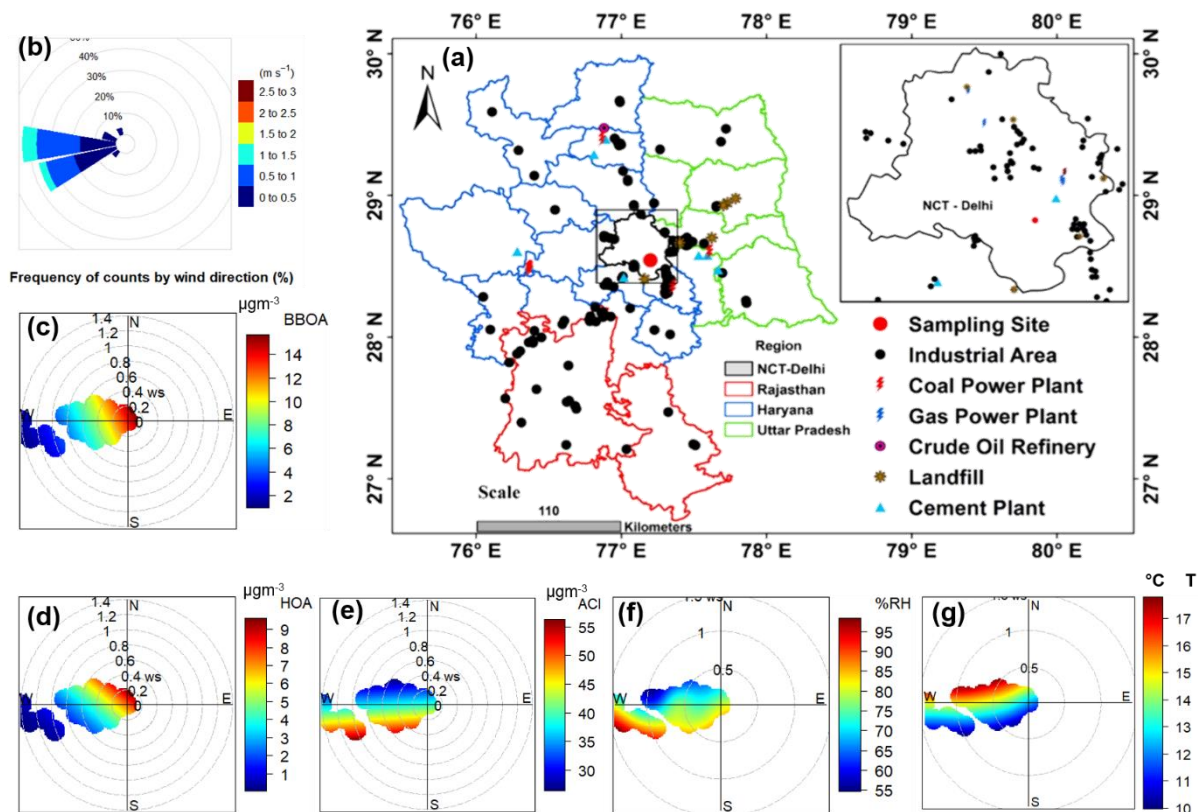
Figure 7 Map of (a) Delhi showing various types of industries located in the region and nearby locations, (b) wind rose diagram and conditional bi-polar plots showing variation in mass concentration of (c) biomass burning OA (BBOA), (d) hydrocarbon like OA (HOA), (e) ammonium chloride (ACl), (f) % ambient relative humidity (RH), and (g) ambient temperature (T), with wind direction (WD) and wind speed (WS) during H-Cl events. A background map showing various industrial locations was adapted from Rai et al. (2020).

3.2.4.2 High biomass burning (H-BB) Events

During the initial period of the field campaign (1-12 February), there were instances of high BB events. However, H-BB events were generally observed during the midnight (01:00 hours) to morning (08:00 hours) or evening (20:00 hours) to midnight (01:00 hours), and occasionally from evening (21:00 hours) to morning (11:00 hours). The surface wind circulations were predominantly from the W, W-WNW, and W-WSW directions (refer to Fig. S9b). The aerosol in this study was primarily sourced from local emissions. The aerosol constituents were mainly associated with slower wind circulations from landfill sites, industrial areas, and coal power plants, as shown in Fig. S9a. The PSCF analysis was justified by considering 48-hour air mass back trajectories, as shown in Fig. S10. The average GMD of the PNSD was nearly 87 nm. Additionally, the mean concentration of SO_2, NOx, and CO were at 4.7 ppb, 124.1 ppb, and 1.5 ppm, respectively. Therefore, it is possible that BBOA was contributed from the open local biomass burning activities at landfill sites or others sources. The H-BB event showed that

organic aerosol confined the largest fraction of BBOA, at 39%, followed by HOA at 28%. Fig. S9 (b, c, and d) clearly shows that BBOA and HOA have similar local source profiles but differ from the ACl source. Additionally, ACl was not found to have a strong association with ambient RH, but it was associated with emissions from a nearby coal power plant. However, the 48-hour air mass back trajectories indicate that the current city is also influenced by air masses from certain parts of Uttar Pradesh, Punjab, and Haryana. These states are potential hubs for crop residue burning, industrial activities and brick kilns, which contribute significantly to the presence of organic aerosols in PM_1, particularly during winter. The H-BB event captured a significant volume fraction, 71%, of OA in PM_1. BBOA contributed almost 39%, as shown in Fig. 9. A lower inorganic to OA ratio was a potential factor in decreasing the aerosol hygroscopicity during H-BB events. Additionally, the contribution of primary organic aerosol was enhanced during this event and, on average, increased to 67%. The hygroscopicity of the aerosol is inversely affected by organic aerosol loading. This observation was also reported by Mandariya et al. (2020) in Kanpur. The authors suggested that the hygroscopicity of the aerosol is adversely affected by primary biomass burning (BBOA) and hydrocarbon-like OA. BBOA was found to have a strong negative correlation with the hygroscopicity of 200 nm particles, supporting the conclusion. Apart from this, the Nucleation size particle (20 nm) exhibited a hygroscopicity parameter of 0.02 ± 0.02 with a mono mode GF-PDF with the unit mode (Fig. 8b) and consisted of $83.7 \pm 18.6\%$ nearly hydrophobic particles. Additionally, as the aerosol size increased, the hygroscopicity parameter ($\kappa_{H\text{-}TDMA\_90\%}$) significantly ($p<0.05$) increased due to the contribution of relatively secondary aerosol particles (GF>1.2) with increasing aerosol size. Approximately 54% of the accumulation size aerosol with a diameter of 100 nm is contributed by nearly hydrophobic particles (GF<1.2), while the remaining 46% is contributed by more hygroscopic particles (GF>1.2).

3.2.4.3 High-HOA (H-HOA) Events

H-HOA events were identified based on the considerable mass concentration and fraction of HOA in the organic aerosol. These periods were generally noted from19:00 hr to 09:00 hr the following morning during February 22-23, February 26-27 February, March 4, and March 7-8, as indicated in Fig. 2. The average geometric mean diameter of the particle number size distribution was nearly 80 nm. Additionally, the mean concentrations of SO_2, NOx, and CO 4.3 ppb, 136.7 ppb, and 1.1 ppm, respectively. The potential impact of long-range transported aerosol was explored using PSCF. Air masses over Delhi, Haryana, and Uttar Pradesh were found to be potentially associated with hydrocarbon-like organic aerosols (Fig. S11). BBOA also followed a similar path as HOA. However, the potential area source of ACl was the nearby region of Delhi and Haryana. The loading of HOA was significantly ($p<0.05$) higher than in H-BB, H-Cl and Clean periods. However, emission sources were different

547 during both H-HOA and H-BB periods. HOA may be a critical constituent in modulating aerosol hygroscopicity

548 during these events, as it has been identified as a potential contributor to OA. HOA is typically considered

549 hydrophobic (Duplissy et al., 2011), and therefore, its elevated contribution (41%) to OA could be responsible for

550 the lower κ observed during these events. The overall hygroscopicity of particles with sizes of 20, 50, 100, 150,

551 and 200 nm was recorded as 0.01 ± 0.01, 0.06 ± 0.03, 0.11 ± 0.03, 0.14 ± 0.04, and 0.17 ± 0.05, respectively. The

552 lower hygroscopicity of particles may be attributed to the predominant fractional contribution of primary aerosol

553 particles (GF<1.2), as illustrated in Fig. 7(c). In general, OA constitutes the majority of the PM_1, with primary

554 OA accounting for approximately 60% of the OA. However, the relative increase in the contribution of other more

555 hygroscopic constituents, such as secondary organic aerosol (LO-OOA and MO-OOA), ACl, and AS, in the

556 aerosol may help to balance the negative impact of high-HOA, which is limited by κ.

557 **3.2.4.5 Relatively Clean Period**

558 Clean events were recorded on February 24th, 25th, and March 5th-7th. The clean duration was from 9 PM to 11

559 AM. E and S-E winds dominated the relatively clean period, but pollution was associated with calm winds, as

560 shown in Fig. S9. The average GMD of the PNSD was nearly 54 nm. Additionally, the mean concentrations of

561 SO_2, NOx, and CO concentrations were at 4.2 ppb, 43.2 ppb, and 0.4 ppm, respectively. Similar sources were

562 found for BBOA, HOA, and ACl, and they were all strongly associated with ambient relative humidity. The mean

563 concentrations of organic aerosol, ACl, AN, and AS were 11.0 ± 6.4, 1.4 ± 1.1, 3.0 ± 1.5, and 4.4 ± 2.2 $\mu g m^{-3}$,

564 respectively. These mass concentrations were significantly lower than in other specified periods. However, OA

565 was still the dominant species, comprising 56% of the PM_1 volume, as shown in Fig. 9. Of all the factors

566 contributing to OA, HOA was the dominant, accounting for 33%. However, secondary organic aerosol accounted

567 for the majority of OA at 54.4%. Secondary OA is characterize by a relatively higher degree of oxidation, which

568 positively affects OA hygroscopicity (Kim et al., 2017; Richard et al., 2011; Wu et al., 2013a). The mean

569 hygroscopicity of particles with diameters of 20, 50, 100, 150, and 200 nm during the Clean period were observed

570 to be 0.03 ± 0.02, 0.09 ± 0.04, 0.14 ± 0.06, 0.22 ± 0.09, and 0.27 ± 0.07, respectively. These values were

571 significantly ($p<0.05$) different from each other. However, the hygroscopicity of the 200 nm accumulation

572 particles was not significantly ($p>0.05$) higher than that of the 150 nm particles. The increase in hygroscopicity

573 as particle size increases from 20 to 200 nm can also be attributed to the greater proportion of more hygroscopic

574 particles (GF>1.2) compared to nearly hydrophobic or less hygroscopic particles (GF<1.2). The nucleation

575 particles, with a size of 20 nm, were mostly composed of less hygroscopic particles ($76.8 \pm 21.7\%$). This indicates

576 that there was an influence from fresh emission sources. On the other hand, Aitken (50 nm) and Accumulation

577 (200 nm) size aerosols had a lower percentage of less hygroscopic particles, with 69.3 ± 14.7 and 25.4 ± 10.8,

578 respectively. These results suggest that accumulation-size aerosols dominated secondary aerosols, which is also

579 supported by their GF-PDF as shown in Fig. 8(a). Aerosol particles of nucleation size (20nm) exhibited a nearly

580 mono-modal GF-PDF with a mode of unit growth factor. In contrast, as the aerosol size increased, the mode

581 shifted towards the higher end and the GF-PDF shifted from unit to multi-mode.
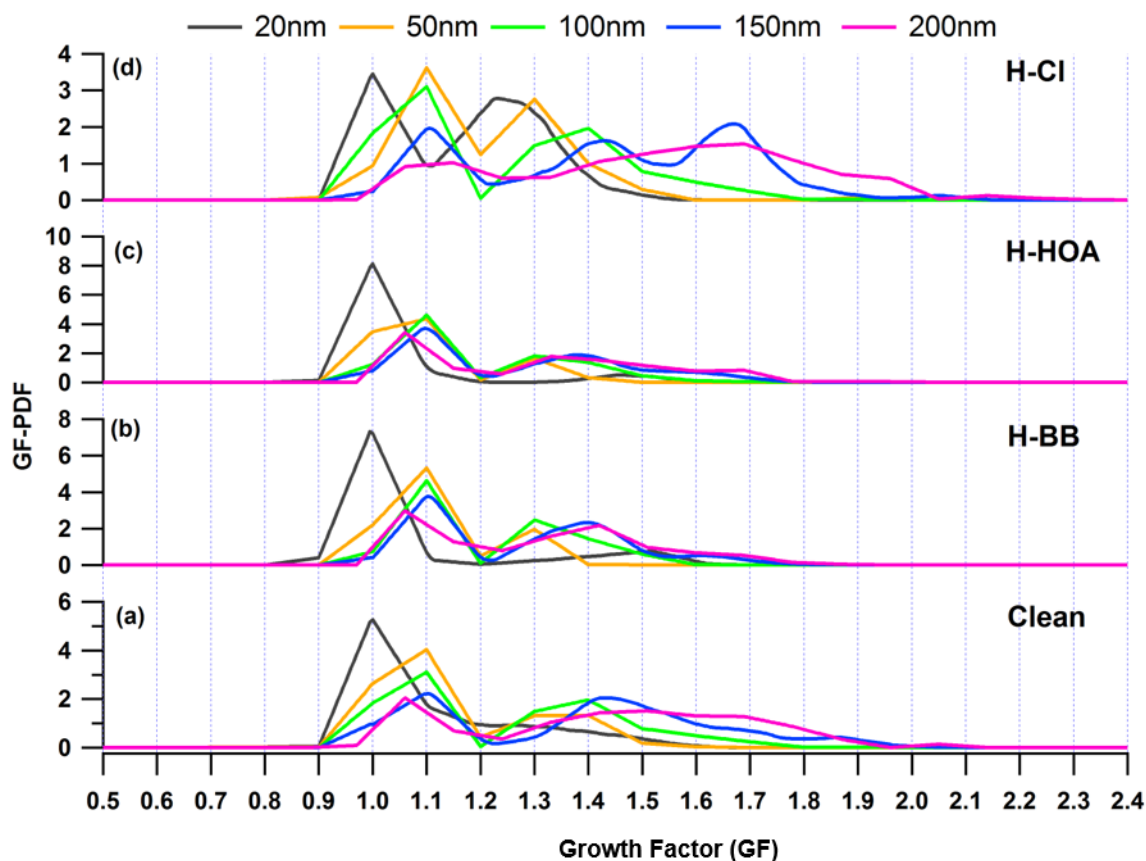
582

583 **Figure 8: Growth Factor Probability Density Function (GF-PDF) of 20, 50, 100, 150, and 200 nm aerosol particles for**

584 **the (a) clean, (b) H-BB, (c) H-HOA, and H-Cl periods.**

585 **3.2.4.6 Comparison of κ for different events**

586 We compared the hygroscopicity of aerosols during different periods using a 200 nm particle size that represents

587 the bulk aerosol chemical composition. Additionally, in this study, the mode of the particle-volume size

588 distribution ranged from 400 nm to 600 nm in dry mobility diameter. Therefore, 200 nm particles are the best

589 choice for comparing hygroscopicity parameters among different periods, considering bulk aerosol composition.

590 Additionally, a good Pearson's r value of 0.76 was found between $\kappa_{200nm\_90\%}$ and $\kappa_{chem\_90\%}$, which were derived

25

591   from the chemical composition of dry PM_1 particles measured by the ACSM using the ZSR mixing rule (Stokes

592   and Robinson, 1966). This support our selection.

593   The event labeled H-Cl exhibited the highest value (0.36 ± 0.06) of $\kappa_{200nm\_90\%}$ compared to the events labeled H-

594   BB (0.18 ± 0.04), H-HOA (0.17 ± 0.05), and Clean (0.27 ± 0.07), as shown in Fig. 9. Additionally, the average

595    $\kappa_{200nm\_90\%}$ value for the H-Cl event was significantly ($p<0.05$) higher than that of the other events. A significant

596   increase in Cl emissions in the Delhi region could lead to a substantial increase in the aerosol liquid water content.

597   This increase in water content could result in higher aerosol hygroscopicity, which could further enhance cloud

598   condensation nuclei formation. This, in turn, could potentially trigger haze/fog events in Delhi NCR (Gunthe et

599   al., 2021). Controlling open trash/waste burning in the region could help minimize Cl emissions, which in turn

600   could rduce the possibility of haze/fog formation during high atmospheric conditions. However, there was no

601   significant difference ($p>0.05$) in $\kappa_{200nm\_90\%}$ values between H-BB and H-HOA events, possibly due to relative

602   changes in primary, secondary OA, and inorganic species. In H-HOA events, the negative effect of a significantly

603   higher fractional contribution of HOA to OA (41%) possibly balances with a positive impact of a 7% increase in

604   secondary OA relative to H-BB. Several worldwide studies (Jimenez et al., 2009; Mandariya et al., 2019; Sun et

605   al., 2013) have reported that secondary organic aerosol is associated with a higher O/C ratio. Additionally, several

606   studies have found a positive correlation between the O/C ratio and κ (Jimenez et al., 2009; Kim et al., 2020), as

607   described earlier. Furthermore, a 5% decrease in ACl during H-HOA events may be offset by a 7% increase in

608   AS fraction during H-BB events. Overall, the relative changes in aerosol constituents resulted in insignificant

609   changes in κ during H-BB and H-HOA periods. However, H-BB and H-HOA events showed significantly

610   ($p<0.05$) lower hygroscopicity compared to a relatively cleaner atmosphere. The aerosol associated with relatively

611   cleaner events had a higher inorganic-to-organic ratio. Additionally, during clean periods, the aerosol consisted

612   of a significantly higher fraction of secondary organic aerosol. This could be the reason for the higher

613   hygroscopicity associated with organic aerosol compared to other events. Studies worldwide (Aiken et al., 2008;

614   Cerully et al., 2015b; Chakraborty et al., 2016b; Mandariya et al., 2019) have reported that organic aerosol loading

615   has an inverse impact on the oxidation/aging process of OA. This results in higher hygroscopicity during relatively

616   cleaner periods.
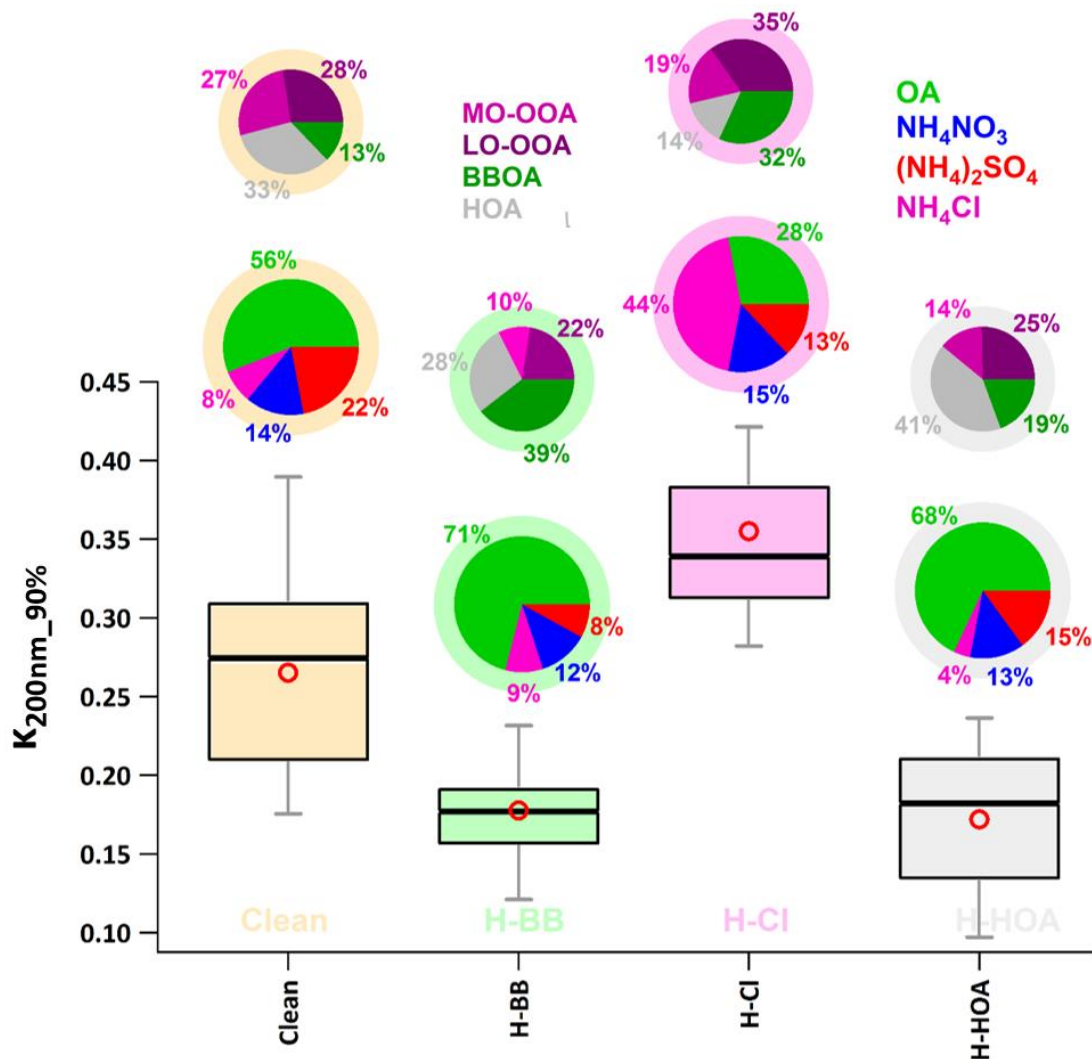
Figure 9: Box plot showing variation in H-TDMA measured hygroscopic parameter of 200 nm size particles $\kappa_{\text{H-TDMA}}$ ($\kappa_{\text{200nm\_90\%}}$) in high biomass burning (H-BB), high-chloride (H-Cl), and high-hydrocarbon like organic aerosol (H-HOA) events. Different colors represent respective events in the plot. A bigger pie chart represents the overall average volume fractional contribution of various aerosol species indicated by color-coding. In addition, minor pie charts described the event average mass fractional contribution of different OA species in OA. Diffused ring color of the pie chart displays the respective event.

4. Conclusions

The study examined the hygroscopicity of aerosol particles of various sizes (Nucleation - 20 nm, Aitken - 50 nm, and Accumulation - 150 and 200 nm) in Delhi during the winter months of February-March 2020. The research also identified differences in hygroscopicity, particularly in aerosols with higher levels of chloride, biomass burning, and hydrocarbon-like organic components. Delhi is known as one of the most polluted cities, particularly

during winter haze and fog events when it often experiences high levels of chloride pollution. This study reports on the temporal variations in size-specific hygroscopic parameters ($\kappa_{\text{H-TDMA\_90\%}}$) under sub-saturated conditions (90% RH) in Delhi for the first time. Additionally, it presents the hygroscopicity of nucleation and Aitken mode particles using HTDMA for the first time in India.

The $\kappa_{\text{H-TDMA\_90\%}}$ values observed for aerosol particles of 20 nm, 50 nm, 100 nm, 150 nm, and 200 nm ranged from 0.00 to 0.11 (with an average of 0.03 ± 0.02), 0.05 to 0.22 (0.11 ± 0.03), 0.05 to 0.30 (0.14 ± 0.04), 0.05 to 0.41 (0.18 ± 0.06), and 0.05 to 0.56 (0.22 ± 0.07), respectively. During the study period, it was observed that the average hygroscopicity parameter increased significantly with the size of the particles ($p<0.05$). The diurnal variations of $\kappa_{\text{20nm\_90\%}}$ and $\kappa_{\text{50nm\_90\%}}$ were dynamic, while larger accumulation mode particles showed a flatter diurnal pattern. This was due to the positive and negative effects of changes in the volume fraction of NH_4Cl and organic aerosol in the aerosol with increasing particle size. The variation in $\kappa_{\text{200nm\_90\%}}$ was primarily associated with fluctuations in NH_4Cl and OA, rather than $(NH_4)_2SO_4$. It is important to note that this evaluation is based on objective data and does not include any subjective evaluations

Pollution episodes were mainly linked to local biomass burning and industrial and waste-burning emissions in Delhi and nearby regions. The study primarily focused on the impacts of high biomass burning (H-BB), high hydrocarbon-like OA (H-HOA), and high chloride emissions (H-Cl) on aerosol hygroscopicity and compared them to cleaner periods. The period with H-Cl exhibited significantly higher hygroscopicity (0.35 ± 0.06) compared to the periods with H-BB (0.18 ± 0.04), H-HOA (0.17 ± 0.05), and the relatively cleaner period (0.27 ± 0.07). However, H-BB and H-HOA showed no significant difference in hygroscopicity but displayed lower hygroscopicity compared to the cleaner periods. This could be attributed to lower levels of organic aerosols and a higher ratio of inorganic-to-organic aerosol in the aerosol. The study found that an increase of 10% increase in chloride aerosol (ammonium chloride) significantly increased hygroscopicity, resulting in approximately 3 µg m^{-3} higher aerosol liquid water content during high chloride events. This 10% increase in a high-volume fraction of ammonium chloride in aerosol significantly ($p<0.05$) enhanced aerosol hygroscopicity by 0.0041. The research indicates that chloride emissions are a significant concern in Delhi. These emissions enhance aerosol hygroscopicity, promote cloud formation during winter days, and contribute to fog and haze in the region. High levels of chloride in aerosols counteract the negative impact of high organic aerosol loading on cloud condensation nuclei activity. The study suggests that controlling open burning of waste materials could help reduce haze and fog events in Delhi during the winter months.

658 **Supporting Information**

659 Supplementary pieces of information are mentioned in the supplementary file.

660 **Data availability.** Data can be accessed at the following repository:

661 https://web.iitd.ac.in/~gazala/publications.html (Mandariya et al., 2023).

662 **Author contributions.** AKM: conceptualization, HTDMA data analysis, investigation, methodology, writing
663 (original draft and review and editing). AA: operated aerosol instrumentation and collection of data on-board in
664 Delhi, analysis of MPSS data, conceptualization, conceptualization, review and editing. MMVH: help in data
665 collection. NAB: ACSM operation and data collection. KP: ACSM data analysis and PMF analysis. JSA:
666 providing ACSM, review, and editing. LHR: ACSM, review, and editing. AW: experiment design, project
667 administration, supervision, review, and editing. GH: operated aerosol instrumentation and collection of data on-
668 board in Delhi, data analysis, methodology, funding acquisition, project administration, supervision, review and
669 editing.

670 **Corresponding Author**

671 Gazala Habib (gazalahabib@civil.iitd.ac.in) and Alfred Wiedensohler (ali@tropos.de)

672 **Competing interests**

673 The authors declare that they have no conflict of interest.

674

675 **Acknowledgment**

676 The authors express their gratitude to Dr. Martin Gysel of the Aerosol Physics Group at the Paul Scherrer Institute

677 in Switzerland for providing the TDMAinv toolkit for HTDMA data correction.

678 **REFERENCES**

679 Achtert, P., Birmili, W., Nowak, A., Wehner, B., Wiedensohler, A., Takegawa, N., Kondo, Y., Miyazaki, Y., Hu,
680 M. and Zhu, T.: Hygroscopic growth of tropospheric particle number size distributions over the North China Plain,
681 J. Geophys. Res., 114(8), D00G07, doi:10.1029/2008JD010921, 2009.

682 Aiken, A. C., Decarlo, P. F., Kroll, J. H., Worsnop, D. R., Huffman, J. A., Docherty, K. S., Ulbrich, I. M., Mohr,
683 C., Kimmel, J. R., Sueper, D., Sun, Y., Zhang, Q., Trimborn, A., Northway, M., Ziemann, P. J., Canagaratna, M.
684 R., Onasch, T. B., Alfarra, M. R., Prevot, A. S. H., Dommen, J., Duplissy, J., Metzger, A., Baltensperger, U. and
685 Jimenez, J. L.: O/C and OM/OC ratios of primary, secondary, and ambient organic aerosols with high-resolution
686 time-of-flight aerosol mass spectrometry, Environ. Sci. Technol., 42(12), 4478–4485, doi:10.1021/es703009q,
687 2008.

688   Albrecht, B. A.: Aerosols, Cloud Microphysics, and Fractional Cloudiness, Science (80-.)., 245(4923), 1227–
689   1230, doi:10.1126/science.245.4923.1227, 1989.

690   Arub, Z., Bhandari, S., Gani, S., Apte, J. S., Hildebrandt Ruiz, L. and Habib, G.: Air mass physiochemical
691   characteristics over New Delhi: impacts on aerosol hygroscopicity and cloud condensation nuclei (CCN)
692   formation, Atmos. Chem. Phys., 20(11), 6953–6971, doi:10.5194/acp-20-6953-2020, 2020.

693   Bhandari, S., Gani, S., Patel, K., Wang, D. S., Soni, P., Arub, Z., Habib, G., Apte, J. S. and Hildebrandt Ruiz, L.:
694   Sources and atmospheric dynamics of organic aerosol in New Delhi, India: insights from receptor modeling,
695   Atmos. Chem. Phys., 20(2), 735–752, doi:10.5194/acp-20-735-2020, 2020.

696   Bhattu, D. and Tripathi, S. N.: CCN closure study: Effects of aerosol chemical composition andmixing state, J.
697   Geophys. Res., 120(2), 766–783, doi:10.1002/2014JD021978, 2015.

698   Bhattu, D., Tripathi, S. N. and Chakraborty, A.: Deriving aerosol hygroscopic mixing state from size-resolved
699   CCN   activity   and   HR-ToF-AMS   measurements,   Atmos.   Environ.,   142,   57–70,
700   doi:10.1016/j.atmosenv.2016.07.032, 2016.

701   Cerully, K. M., Bougiatioti, A., Hite, J. R., Guo, H., Xu, L., Ng, N. L., Weber, R. and Nenes, A.: On the link
702   between hygroscopicity, volatility, and oxidation state of ambient and water-soluble aerosols in the southeastern
703   United States, Atmos. Chem. Phys., 15(15), 8679–8694, doi:10.5194/acp-15-8679-2015, 2015a.

704   Cerully, K. M., Bougiatioti, A., Hite, J. R., Guo, H., Xu, L., Ng, N. L., Weber, R. and Nenes, A.: On the link
705   between hygroscopicity, volatility, and oxidation state of ambient and water-soluble aerosols in the southeastern
706   United States, Atmos. Chem. Phys., 15(15), 8679–8694, doi:10.5194/acp-15-8679-2015, 2015b.

707   Chakraborty, A., Gupta, T. and Tripathi, S. N.: Combined effects of organic aerosol loading and fog processing
708   on organic aerosols oxidation, composition, and evolution, Sci. Total Environ., 573, 690–698,
709   doi:10.1016/j.scitotenv.2016.08.156, 2016a.

710   Chakraborty, A., Gupta, T. and Tripathi, S. N.: Combined effects of organic aerosol loading and fog processing
711   on organic aerosols oxidation, composition, and evolution, Sci. Total Environ., 573, 690–698,
712   doi:10.1016/j.scitotenv.2016.08.156, 2016b.

713   Chen, Y., Wang, Y., Nenes, A., Wild, O., Song, S., Hu, D., Liu, D., He, J., Hildebrandt Ruiz, L., Apte, J. S.,
714   Gunthe, S. S. and Liu, P.: Ammonium Chloride Associated Aerosol Liquid Water Enhances Haze in Delhi, India,
715   Environ. Sci. Technol., 56(11), 7163–7173, doi:10.1021/ACS.EST.2C00650, 2022.

716   Draxler, Roland R., Hess, G. D.: Descrpition of the HYSPLIT_4 Modeling System, NOAA Techinical Memo.
717   ERL ARL-224, (October 2004), 28 [online] Available from: http://arlsun.arlhq.noaa.gov/documents/reports/arl-
718   224.pdf%5Cnhttp://www.ciecem.uhu.es/hysplitweb08/document/arl-224.pdf, 1997.

719   Duplissy, J., De Carlo, P. F., Dommen, J., Alfarra, M. R., Metzger, A., Barmpadimos, I., Prevot, A. S. H.,
720   Weingartner, E., Tritscher, T., Gysel, M., Aiken, A. C., Jimenez, J. L., Canagaratna, M. R., Worsnop, D. R.,
721   Collins, D. R., Tomlinson, J. and Baltensperger, U.: Relating hygroscopicity and composition of organic aerosol
722   particulate matter, Atmos. Chem. Phys., 11(3), 1155–1165, doi:10.5194/acp-11-1155-2011, 2011.

723   Enroth, J., Mikkilä, J., Németh, Z., Kulmala, M. and Salma, I.: Wintertime hygroscopicity and volatility of
724   ambient urban aerosol particles, Atmos. Chem. Phys., 18(7), 4533–4548, doi:10.5194/acp-18-4533-2018, 2018.

725   Ervens, B., Turpin, B. J. and Weber, R. J.: Secondary organic aerosol formation in cloud droplets and aqueous
726   particles (aqSOA): A review of laboratory, field and model studies, Atmos. Chem. Phys., 11(21), 11069–11102,
727   doi:10.5194/acp-11-11069-2011, 2011.

728   Fan, X., Liu, J., Zhang, F., Chen, L., Collins, D., Xu, W., Jin, X., Ren, J., Wang, Y., Wu, H., Li, S., Sun, Y. and
729   Li, Z.: Contrasting size-resolved hygroscopicity of fine particles derived by HTDMA and HR-ToF-AMS
730   measurements between summer and winter in Beijing: the impacts of aerosol aging and local emissions, Atmos.
731   Chem. Phys., 20(2), 915–929, doi:10.5194/acp-20-915-2020, 2020.

732   Fountoukis, C. and Nenes, A.: ISORROPIAII: A computationally efficient thermodynamic equilibrium model for

K+-Ca2+-Mg2+-NH4+-Na+-SO42--NO3--Cl--H2O aerosols, Atmos. Chem. Phys., 7(17), 4639–4659, doi:10.5194/acp-7-4639-2007, 2007.

Gani, S., Bhandari, S., Seraj, S., Wang, D. S., Patel, K., Soni, P., Arub, Z., Habib, G., Hildebrandt Ruiz, L. and Apte, J. S.: Submicron aerosol composition in the world's most polluted megacity: the Delhi Aerosol Supersite study, Atmos. Chem. Phys., 19(10), 6843–6859, doi:10.5194/acp-19-6843-2019, 2019.

Gunthe, S. S., Rose, D., Su, H., Garland, R. M., Achtert, P., Nowak, A., Wiedensohler, A., Kuwata, M., Takegawa, N., Kondo, Y., Hu, M., Shao, M., Zhu, T., Andreae, M. O. and Pöschl, U.: Cloud condensation nuclei (CCN) from fresh and aged air pollution in the megacity region of Beijing, Atmos. Chem. Phys., 11(21), 11023–11039, doi:10.5194/acp-11-11023-2011, 2011.

Gunthe, S. S., Liu, P., Panda, U., Raj, S. S., Sharma, A., Darbyshire, E., Reyes-Villegas, E., Allan, J., Chen, Y., Wang, X., Song, S., Pöhlker, M. L., Shi, L., Wang, Y., Kommula, S. M., Liu, T., Ravikrishna, R., McFiggans, G., Mickley, L. J., Martin, S. T., Pöschl, U., Andreae, M. O. and Coe, H.: Enhanced aerosol particle growth sustained by high continental chlorine emission in India, Nat. Geosci., 14(2), 77–84, doi:10.1038/s41561-020-00677-x, 2021.

Gupta, T. and Mandariya, A.: Sources of submicron aerosol during fog-dominated wintertime at Kanpur, Environ. Sci. Pollut. Res., 20(8), doi:10.1007/s11356-013-1580-6, 2013.

Gysel, M., Crosier, J., Topping, D. O., Whitehead, J. D., Bower, K. N., Cubison, M. J., Williams, P. I., Flynn, M. J., McFiggans, G. B. and Coe, H.: Closure study between chemical composition and hygroscopic growth of aerosol particles during TORCH2, Atmos. Chem. Phys., 7(24), 6131–6144, doi:10.5194/acp-7-6131-2007, 2007.

Gysel, M., McFiggans, G. B. and Coe, H.: Inversion of tandem differential mobility analyser (TDMA) measurements, J. Aerosol Sci., 40(2), 134–151, doi:10.1016/j.jaerosci.2008.07.013, 2009.

Hallquist, M., Wenger, J. C., Baltensperger, U., Rudich, Y., Simpson, D., Claeys, M., Dommen, J., Donahue, N. M., George, C., Goldstein, A. H., Hamilton, J. F., Herrmann, H., Hoffmann, T., Linuma, Y., Jang, M., Jenkin, M. E., Jimenez, J. L., Kiendler-Scharr, A., Maenhaut, W., McFiggans, G., Mentel, T. F., Monod, A., Prévôt, A. S. H., Seinfeld, J. H., Surratt, J. D., Szmigielski, R. and Wildt, J.: The formation, properties and impact of secondary organic aerosol: current and emerging issues, Atmos. Chem. Phys., 9(November 2008), 5155–5236, 2009.

Hong, J., Häkkinen, S. A. K., Paramonov, M., Äijälä, M., Hakala, J., Nieminen, T., Mikkilä, J., Prisle, N. L., Kulmala, M., Riipinen, I., Bilde, M., Kerminen, V. M. and Petäjä, T.: Hygroscopicity, CCN and volatility properties of submicron atmospheric aerosol in a boreal forest environment during the summer of 2010, Atmos. Chem. Phys., 14(9), 4733–4748, doi:10.5194/acp-14-4733-2014, 2014.

Hong, J., Kim, J., Nieminen, T., Duplissy, J., Ehn, M., Äijälä, M., Hao, L. Q., Nie, W., Sarnela, N., Prisle, N. L., Kulmala, M., Virtanen, A., Petäjä, T. and Kerminen, V. M.: Relating the hygroscopic properties of submicron aerosol to both gas- and particle-phase chemical composition in a boreal forest environment, Atmos. Chem. Phys., 15(20), 11999–12009, doi:10.5194/acp-15-11999-2015, 2015.

Hong, J., Xu, H., Tan, H., Yin, C., Hao, L., Li, F., Cai, M., Deng, X., Wang, N., Su, H., Cheng, Y., Wang, L., Petäjä, T. and Kerminen, V. M.: Mixing state and particle hygroscopicity of organic-dominated aerosols over the Pearl River Delta region in China, Atmos. Chem. Phys., 18(19), 14079–14094, doi:10.5194/acp-18-14079-2018, 2018.

Hu, D., Chen, J., Ye, X., Li, L. and Yang, X.: Hygroscopicity and evaporation of ammonium chloride and ammonium nitrate: Relative humidity and size effects on the growth factor, Atmos. Environ., 45(14), 2349–2355, doi:10.1016/j.atmosenv.2011.02.024, 2011.

Intergovernmental Panel on Climate Change: Climate Change 2021 – The Physical Science Basis, Cambridge University Press., 2023.

Jimenez, J. L., Canagaratna, M. R., Donahue, N. M., Prevot, A. S. H., Zhang, Q., Kroll, J. H., DeCarlo, P. F., Allan, J. D., Coe, H., Ng, N. L., Aiken, A. C., Docherty, K. S., Ulbrich, I. M., Grieshop, A. P., Robinson, A. L., Duplissy, J., Smith, J. D., Wilson, K. R., Lanz, V. A., Hueglin, C., Sun, Y. L., Tian, J., Laaksonen, A., Raatikainen,

T., Rautiainen, J., Vaattovaara, P., Ehn, M., Kulmala, M., Tomlinson, J. M., Collins, D. R., Cubison, M. J., Dunlea, E. J., Huffman, J. A., Onasch, T. B., Alfarra, M. R., Williams, P. I., Bower, K., Kondo, Y., Schneider, J., Drewnick, F., Borrmann, S., Weimer, S., Demerjian, K., Salcedo, D., Cottrell, L., Griffin, R., Takami, A., Miyoshi, T., Hatakeyama, S., Shimono, A., Sun, J. Y., Zhang, Y. M., Dzepina, K., Kimmel, J. R., Sueper, D., Jayne, J. T., Herndon, S. C., Trimborn, A. M., Williams, L. R., Wood, E. C., Middlebrook, A. M., Kolb, C. E., Baltensperger, U. and Worsnop, D. R.: Evolution of organic aerosols in the atmosphere, Science (80-.)., 326(5959), 1525–1529, doi:10.1126/science.1180353, 2009.

Kawana, K., Nakayama, T. and Mochida, M.: Hygroscopicity and CCN activity of atmospheric aerosol particles and their relation to organics: Characteristics of urban aerosols in Nagoya, Japan, J. Geophys. Res. Atmos., 121(8), 4100–4121, doi:10.1002/2015JD023213, 2016.

Kecorius, S., Vogl, T., Paasonen, P., Lampilahti, J., Rothenberg, D., Wex, H., Zeppenfeld, S., Van Pinxteren, M., Hartmann, M., Henning, S., Gong, X., Welti, A., Kulmala, M., Stratmann, F., Herrmann, H. and Wiedensohler, A.: New particle formation and its effect on cloud condensation nuclei abundance in the summer Arctic: a case study in the Fram Strait and Barents Sea, Atmos. Chem. Phys, 19, 14339–14364, doi:10.5194/acp-19-14339-2019, 2019.

Kim, N., Park, M., Yum, S. S., Park, J. S., Song, I. H., Shin, H. J., Ahn, J. Y., Kwak, K. H., Kim, H., Bae, G. N. and Lee, G.: Hygroscopic properties of urban aerosols and their cloud condensation nuclei activities measured in Seoul during the MAPS-Seoul campaign, Atmos. Environ., 153, 217–232, doi:10.1016/j.atmosenv.2017.01.034, 2017.

Kim, N., Yum, S. S., Park, M., Park, J. S., Shin, H. J. and Ahn, J. Y.: Hygroscopicity of urban aerosols and its link to size-resolved chemical composition during spring and summer in Seoul, Korea, Atmos. Chem. Phys., 20(19), 11245–11262, doi:10.5194/acp-20-11245-2020, 2020.

Kitamori, Y., Mochida, M. and Kawamura, K.: Assessment of the aerosol water content in urban atmospheric particles by the hygroscopic growth measurements in Sapporo, Japan, Atmos. Environ., 43(21), 3416–3423, doi:10.1016/j.atmosenv.2009.03.037, 2009.

Kroll, J. H., Donahue, N. M., Jimenez, J. L., Kessler, S. H., Canagaratna, M. R., Wilson, K. R., Altieri, K. E., Mazzoleni, L. R., Wozniak, A. S., Bluhm, H., Mysak, E. R., Smith, J. D., Kolb, C. E. and Worsnop, D. R.: Carbon oxidation state as a metric for describing the chemistry of atmospheric organic aerosol, Nat. Chem., 3(2), 133–139, doi:10.1038/nchem.948, 2011.

Li, H., Wang, Q., Shao, M., Wang, J., Wang, C., Sun, Y., Qian, X., Wu, H., Yang, M. and Li, F.: Fractionation of airborne particulate-bound elements in haze-fog episode and associated health risks in a megacity of southeast China, Environ. Pollut., 208, 655–662, doi:10.1016/j.envpol.2015.10.042, 2016.

Liu, J., Horowitz, L. W., Fan, S., Carlton, A. G. and Levy, H.: Global in-cloud production of secondary organic aerosols: Implementation of a detailed chemical mechanism in the GFDL atmospheric model AM3, J. Geophys. Res. Atmos., 117(D15), n/a-n/a, doi:10.1029/2012JD017838, 2012.

Lohmann, U. and Feichter, J.: Global indirect aerosol effects: a review, Atmos. Chem. Phys., 5(3), 715–737, doi:10.5194/acp-5-715-2005, 2005.

Mandariya, A. K., Gupta, T. and Tripathi, S. N.: Effect of aqueous-phase processing on the formation and evolution of organic aerosol (OA) under different stages of fog life cycles, Atmos. Environ., 206(November 2018), 60–71, doi:10.1016/j.atmosenv.2019.02.047, 2019.

Mandariya, A. K., Tripathi, S. N., Gupta, T. and Mishra, G.: Wintertime hygroscopic growth factors (HGFs) of accumulation mode particles and their linkage to chemical composition in a heavily polluted urban atmosphere of Kanpur at the Centre of IGP, India: Impact of ambient relative humidity, Sci. Total Environ., 704, 135363, doi:10.1016/j.scitotenv.2019.135363, 2020a.

Mandariya, A. K., Tripathi, S. N., Gupta, T. and Mishra, G.: Wintertime hygroscopic growth factors (HGFs) of accumulation mode particles and their linkage to chemical composition in a heavily polluted urban atmosphere of Kanpur at the Centre of IGP, India: Impact of ambient relative humidity, Sci. Total Environ., 704, doi:10.1016/j.scitotenv.2019.135363, 2020b.

Massling, A., Leinert, S., Wiedensohler, A. and Covert, D.: Hygroscopic growth of sub-micrometer and one-micrometer aerosol particles measured during ACE-Asia, Atmos. Chem. Phys, 7, 3249–3259 [online] Available from: www.atmos-chem-phys.net/7/3249/2007/ (Accessed 30 October 2022), 2007.

Maßling, A., Wiedensohler, A., Busch, B., Neusüß, C., Neusüß, N., Quinn, P., Bates, T. and Covert, D.: Atmospheric Chemistry and Physics Hygroscopic properties of different aerosol types over the Atlantic and Indian Oceans, Atmos. Chem. Phys, 3, 1377–1397 [online] Available from: www.atmos-chem-phys.org/acp/3/1377/ (Accessed 30 October 2022), 2003.

Massoli, P., Lambe, A. T., Ahern, A. T., Williams, L. R., Ehn, M., Mikkilä, J., Canagaratna, M. R., Brune, W. H., Onasch, T. B., Jayne, J. T., Petäjä, T., Kulmala, M., Laaksonen, A., Kolb, C. E., Davidovits, P. and Worsnop, D. R.: Relationship between aerosol oxidation level and hygroscopic properties of laboratory generated secondary organic aerosol (SOA) particles, Geophys. Res. Lett., 37(24), 1–5, doi:10.1029/2010GL045258, 2010.

McFiggans, G., Artaxo, P., Baltensperger, U., Coe, H., Facchini, M. C., Feingold, G., Fuzzi, S., Gysel, M., Laaksonen, A., Lohmann, U., Mentel, T. F., Murphy, D. M., O'Dowd, C. D., Snider, J. R. and Weingartner, E.: The effect of physical and chemical aerosol properties on warm cloud droplet activation, Atmos. Chem. Phys., 6(9), 2593–2649, doi:10.5194/acp-6-2593-2006, 2006.

McNeill, V. F.: Aqueous organic chemistry in the atmosphere: Sources and chemical processing of organic aerosols, Environ. Sci. Technol., 49(3), 1237–1244, doi:10.1021/es5043707, 2015.

Mei, F., Setyan, A., Zhang, Q. and Wang, J.: CCN activity of organic aerosols observed downwind of urban emissions during CARES, Atmos. Chem. Phys., 13(24), 12155–12169, doi:10.5194/acp-13-12155-2013, 2013.

Ng, N. L., Herndon, S. C., Trimborn, A., Canagaratna, M. R., Croteau, P. L., Onasch, T. B., Sueper, D., Worsnop, D. R., Zhang, Q., Sun, Y. L. and Jayne, J. T.: An Aerosol Chemical Speciation Monitor (ACSM) for routine monitoring of the composition and mass concentrations of ambient aerosol, Aerosol Sci. Technol., 45(7), 780–794, doi:10.1080/02786826.2011.560211, 2011.

Ogawa, S., Setoguchi, Y., Kawana, K., Nakayama, T., Ikeda, Y., Sawada, Y., Matsumi, Y. and Mochida, M.: Hygroscopicity of aerosol particles and CCN activity of nearly hydrophobic particles in the urban atmosphere over Japan during summer, J. Geophys. Res., 121(12), 7215–7234, doi:10.1002/2015JD024636, 2016.

Petit, J. E., Favez, O., Albinet, A. and Canonaco, F.: A user-friendly tool for comprehensive evaluation of the geographical origins of atmospheric pollution: Wind and trajectory analyses, Environ. Model. Softw., 88, 183–187, doi:10.1016/j.envsoft.2016.11.022, 2017.

Petters, M. D. and Kreidenweis, S. M.: A single parameter representation of hygroscopic growth and cloud condensation nucleus activity, Atmos. Chem. Phys. Atmos. Chem. Phys., 7, 1961–1971, doi:10.5194/acp-7-1961-2007, 2007.

Prakash, J., Lohia, T., Mandariya, A. K., Habib, G., Gupta, T. and Gupta, S. K.: Chemical characterization and quantitativ e assessment of source-specific health risk of trace metals in PM1.0 at a road site of Delhi, India, Environ. Sci. Pollut. Res., 25(9), 8747–8764, doi:10.1007/s11356-017-1174-9, 2018.

Pringle, K. J., Tost, H., Pozzer, A., Pöschl, U. and Lelieveld, J.: Global distribution of the effective aerosol hygroscopicity parameter for CCN activation, Atmos. Chem. Phys., 10(12), 5241–5255, doi:10.5194/acp-10-5241-2010, 2010.

Rai, P., Furger, M., El Haddad, I., Kumar, V., Wang, L., Singh, A., Dixit, K., Bhattu, D., Petit, J.-E., Ganguly, D., Rastogi, N., Baltensperger, U., Tripathi, S. N., Slowik, J. G. and Prévôt, A. S. H.: Real-time measurement and source apportionment of elements in Delhi's atmosphere, Sci. Total Environ., 742, 140332, doi:10.1016/j.scitotenv.2020.140332, 2020.

Randall, D A; Wood, R A; Bony, S; Colman, R; Fichefet, T; Fyfe, J; Kattsov, V; Pitman, A; Shukla, J; Srinivasan, J; Stouffer, R J; Sumi, A; Taylor, K. E.: Climate Models and Their Application, Clim. Chang. 2007 Phys. Sci. Basis. Contrib. Work. Gr. I to Fourth Assess. Rep. Intergov. Panel Clim. Chang. Ed. by S. Solomon al., Cambridge Univ. Press. Cambridge, U. K., New York., Chapter 8(United Kingdom: N. p., p.2007. Web.), 590–662, doi:http://www.ipcc.ch/pdf/assessment-report/ar4/wg1/ar4-wg1-chapter8.pdf, 2007.

875   Richard, A., Gianini, M. F. D., Mohr, C., Furger, M., Bukowiecki, N. and Minguill, M. C.: and Physics Source
876   apportionment of size and time resolved trace elements and organic aerosols from an urban courtyard site in
877   Switzerland, , 8945–8963, doi:10.5194/acp-11-8945-2011, 2011.

878   Seinfeld, J. H. and Pandis, S. N.: Atmospheric cemistry and physics: From air pollution to climate change, Second
879   edi., John Wiley & Sons, Inc., 2006.

880   Shukla, A. K., Lalchandani, V., Bhattu, D., Dave, J. S., Rai, P., Thamban, N. M., Mishra, S., Gaddamidi, S.,
881   Tripathi, N., Vats, P., Rastogi, N., Sahu, L., Ganguly, D., Kumar, M., Singh, V., Gargava, P. and Tripathi, S. N.:
882   Real-time quantification and source apportionment of fine particulate matter including organics and elements in
883   Delhi during summertime, Atmos. Environ., 261, 118598, doi:10.1016/J.ATMOSENV.2021.118598, 2021.

884   Sjogren, S., Gysel, M., Weingartner, E., Baltensperger, U., Cubison, M. J. and Coe, H.: Hygroscopic growth and
885   water uptake kinetics of two-phase aerosol particles consisting of ammonium sulfate , adipic and humic acid
886   mixtures, , 38, 157–171, doi:10.1016/j.jaerosci.2006.11.005, 2007.

887   Sjogren, S., Gysel, M., Weingartner, E., Alfarra, M. R., Duplissy, J., Cozic, J., Crosier, J. and Coe, and U. B.:
888   Hygroscopicity of the submicrometer aerosol at the high-alpine site Jungfraujoch, 3580m a.s.l., Switzerland, ,
889   7231–7249, doi:10.5194/acp-12-7231-2012, 2012.

890   Stokes, R. H. and Robinson, R. A.: Interactions in Aqueous Nonelectrolyte Solutions. I. Solute-Solvent Equilibria,
891   J. Phys. Chem., 70(7), 2126–2131, doi:10.1021/j100879a010, 1966.

892   Su, H., Rose, D., Cheng, Y. F., Gunthe, S. S., Massling, A., Stock, M., Wiedensohler, A., Andreae, M. O. and
893   Pöschl, U.: Hygroscopicity distribution concept for measurement data analysis and modeling of aerosol particle
894   mixing state with regard to hygroscopic growth and CCN activation, Atmos. Chem. Phys, 10, 7489–7503,
895   doi:10.5194/acp-10-7489-2010, 2010.

896   Sun, Y., Wang, Z., Fu, P., Jiang, Q., Yang, T., Li, J. and Ge, X.: The impact of relative humidity on aerosol
897   composition and evolution processes during wintertime in Beijing , China, Atmos. Environ., 77, 927–934,
898   doi:10.1016/j.atmosenv.2013.06.019, 2013.

899   Sun, Y., Du, W., Fu, P., Wang, Q., Li, J., Ge, X., Zhang, Q., Zhu, C., Ren, L., Xu, W., Zhao, J., Han, T., Worsnop,
900   D. R. and Wang, Z.: Primary and secondary aerosols in Beijing in winter: Sources, variations and processes,
901   Atmos. Chem. Phys., 16(13), 8309–8329, doi:10.5194/acp-16-8309-2016, 2016.

902   Swietlicki, E., Hansson, H. C., Hämeri, K., Svenningsson, B., Massling, A., Mcfiggans, G., Mcmurry, P. H.,
903   Petäjä, T., Tunved, P., Gysel, M., Topping, D., Weingartner, E., Baltensperger, U., Rissler, J., Wiedensohler, A.
904   and Kulmala, M.: Hygroscopic properties of submicrometer atmospheric aerosol particles measured with H-
905   TDMA instruments in various environments—a review, Tellus B Chem. Phys. Meteorol., 60(3), 432–469,
906   doi:10.1111/j.1600-0889.2008.00350.x, 2008.

907   Tang, I. N. and Munkelwitz, H. R.: Water activities, densities, and refractive indices of aqueous sulfates and
908   sodium nitrate droplets of atmospheric importance, J. Geophys. Res., 99(D9), 18801, doi:10.1029/94JD01345,
909   1994.

910   Tobler, A., Bhattu, D., Canonaco, F., Lalchandani, V., Shukla, A., Thamban, N. M., Mishra, S., Srivastava, A. K.,
911   Bisht, D. S., Tiwari, S., Singh, S., Močnik, G., Baltensperger, U., Tripathi, S. N., Slowik, J. G. and Prévôt, A. S.
912   H.: Chemical characterization of PM2.5 and source apportionment of organic aerosol in New Delhi, India, Sci.
913   Total Environ., 745, 140924, doi:10.1016/J.SCITOTENV.2020.140924, 2020.

914   Topping, D. O. and McFiggans, G.: Tight coupling of particle size, number and composition in atmospheric cloud
915   droplet activation, Atmos. Chem. Phys., 12(7), 3253–3260, doi:10.5194/acp-12-3253-2012, 2012.

916   Tritscher, T., Jurnyi, Z., Martin, M., Chirico, R., Gysel, M., Heringa, M. F., Decarlo, P. F., Sierau, B., Prévt, A.
917   S. H., Weingartner, E. and Baltensperger, U.: Changes of hygroscopicity and morphology during ageing of diesel
918   soot, Environ. Res. Lett., 6(3), doi:10.1088/1748-9326/6/3/034026, 2011.

919   Wang, X., Shen, X. J., Sun, J. Y., Zhang, X. Y., Wang, Y. Q., Zhang, Y. M., Wang, P., Xia, C., Qi, X. F. and
920   Zhong, J. T.: Size-resolved hygroscopic behavior of atmospheric aerosols during heavy aerosol pollution episodes

921   in Beijing in December 2016, , 194(September), 188–197, doi:10.1016/j.atmosenv.2018.09.041, 2018a.

922   Wang, Y., Wu, Z., Ma, N., Wu, Y., Zeng, L., Zhao, C. and Wiedensohler, A.: Statistical analysis and
923   parameterization of the hygroscopic growth of the sub-micrometer urban background aerosol in Beijing, Atmos.
924   Environ., 175(December 2017), 184–191, doi:10.1016/j.atmosenv.2017.12.003, 2018b.

925   Wester, P., Mishra, A., Mukherji, A., Shrestha, A. B. and Change, C.: The Hindu Kush Himalaya Assessment,
926   edited by P. Wester, A. Mishra, A. Mukherji, and A. B. Shrestha, Springer International Publishing, Cham., 2019.

927   Wu, Z. J., Poulain, L., Henning, S., Dieckmann, K., Birmili, W., Merkel, M., van Pinxteren, D., Spindler, G.,
928   Müller, K., Stratmann, F., Herrmann, H. and Wiedensohler, A.: Relating particle hygroscopicity and CCN activity
929   to chemical composition during the HCCT-2010 field campaign, Atmos. Chem. Phys., 13(16), 7983–7996,
930   doi:10.5194/acp-13-7983-2013, 2013a.

931   Wu, Z. J., Poulain, L., Henning, S., Dieckmann, K., Birmili, W., Merkel, M., Van Pinxteren, D., Spindler, G.,
932   Stratmann, F., Herrmann, H. and Wiedensohler, A.: Sciences ess Atmospheric Chemistry and Physics Climate of
933   the Past Geoscientific Instrumentation Methods and Data Systems Relating particle hygroscopicity and CCN
934   activity to chemical composition during the HCCT-2010 field campaign, Atmos. Chem. Phys, 13, 7983–7996,
935   doi:10.5194/acp-13-7983-2013, 2013b.

936   Wu, Z. J., Zheng, J., Shang, D. J., Du, Z. F., Wu, Y. S., Zeng, L. M., Wiedensohler, A. and Hu, M.: Particle
937   hygroscopicity and its link to chemical composition in the urban atmosphere of Beijing , China , during
938   summertime, , 1123–1138, doi:10.5194/acp-16-1123-2016, 2016.

939   Yeung, M. C., Lee, B. P., Li, Y. J. and Chan, C. K.: Simultaneous HTDMA and HR-ToF-AMS measurements at
940   the HKUST supersite in Hong Kong in 2011, J. Geophys. Res., 119(16), 9864–9883, doi:10.1002/2013JD021146,
941   2014.

942   Zhang, Q., Jimenez, J. L., Worsnop, D. R. and Canagaratna, M.: A Case Study of Urban Particle Acidity and Its
943   Influence on Secondary Organic Aerosol, Environ. Sci. Technol., 41(9), 3213–3219, doi:10.1021/es061812j,
944   2007.

945   Zhang, S. L., Ma, N., Kecorius, S., Wang, P. C., Hu, M., Wang, Z. B., Größ, J., Wu, Z. J. and Wiedensohler, A.:
946   Mixing state of atmospheric particles over the North China Plain, Atmos. Environ., 125, 152–164,
947   doi:10.1016/J.ATMOSENV.2015.10.053, 2016.

948   Zhang, Y., Tang, L., Yu, H., Wang, Z., Sun, Y., Qin, W., Chen, W., Chen, C., Ding, A., Wu, J., Ge, S. and Chen,
949   C.: Chemical composition , sources and evolution processes of aerosol at an urban site in Yangtze River Delta ,
950   China during wintertime, Atmos. Environ., 123, 339–349, doi:10.1016/j.atmosenv.2015.08.017, 2015.

951   Zhao, P., Du, X., Su, J., Ding, J. and Dong, Q.: Aerosol hygroscopicity based on size-resolved chemical
952   compositions in Beijing, Sci. Total Environ., 716, 137074, doi:10.1016/J.SCITOTENV.2020.137074, 2020.

953